AD_____

Award Number: W81XWH-07-1-0058

TITLE: Cone-Beam Computed Tomography for Image-Guided Radiation Therapy of Prostate Cancer

PRINCIPAL INVESTIGATOR: Seungryong Cho

CONTRACTING ORGANIZATION: University of Chicago
                                              Chicago, IL 60637

REPORT DATE: January 2008

TYPE OF REPORT: Annual Summary

PREPARED FOR: U.S. Army Medical Research and Materiel Command
            Fort Detrick, Maryland 21702-5012

DISTRIBUTION STATEMENT: Approved for Public Release;
                                         Distribution Unlimited

The views, opinions and/or findings contained in this report are those of the author(s) and should not be construed as an official Department of the Army position, policy or decision unless so designated by other documentation.

REPORT DOCUMENTATION PAGE

Form Approved
OMB No. 0704-0188

1. REPORT DATE *(DD-MM-YYYY)* 01-01-2008	2. REPORT TYPE Annual Summary	3. DATES COVERED *(From - To)* 11 DEC 2006 - 11 DEC 2007

4. TITLE AND SUBTITLE

Cone-Beam Computed Tomography for Image-Guided Radiation Therapy of Prostate Cancer

5a. CONTRACT NUMBER

5b. GRANT NUMBER
W81XWH-07-1-0058

5c. PROGRAM ELEMENT NUMBER

6. AUTHOR(S)
Seungryong Cho

E-Mail: srcho@uchicago.edu

5d. PROJECT NUMBER

5e. TASK NUMBER

5f. WORK UNIT NUMBER

7. PERFORMING ORGANIZATION NAME(S) AND ADDRESS(ES)

University of Chicago
Chicago, IL 60637

8. PERFORMING ORGANIZATION REPORT NUMBER

9. SPONSORING / MONITORING AGENCY NAME(S) AND ADDRESS(ES)
U.S. Army Medical Research and Materiel Command
Fort Detrick, Maryland 21702-5012

10. SPONSOR/MONITOR'S ACRONYM(S)

11. SPONSOR/MONITOR'S REPORT NUMBER(S)

12. DISTRIBUTION / AVAILABILITY STATEMENT
Approved for Public Release; Distribution Unlimited

13. SUPPLEMENTARY NOTES

14. ABSTRACT
The success of intensity-modulated radiation therapy (IMRT) or 4-D conformal radiation therapy (CRT) is heavily reliant on accurate image-guidance in prostate cancer treatment. Cone-beam computed tomography (CBCT) is becoming one of the dominant imaging modalities for image-guidance, but current technology based on Feldkamp algorithm for image reconstruction from a circular scanning trajectory does not yield sufficient quality of images. In addition, imaging-radiation dose is one of the key issues, which has to be minimized or optimized. We report innovative CBCT scanning methods and corresponding image reconstruction algorithms that can increase the accuracy of the images and/or reduce patient dose from CBCT. Reverse helical CBCT has been developed, region-of-interest image reconstruction methods have been explored, and a few-view CBCT approach has been proposed.

15. SUBJECT TERMS
Cone-beam computed tomography, image-guided radiation therapy, region-of-interest, few-view

16. SECURITY CLASSIFICATION OF:			17. LIMITATION OF ABSTRACT	18. NUMBER OF PAGES	19a. NAME OF RESPONSIBLE PERSON USAMRMC
a. REPORT U	b. ABSTRACT U	c. THIS PAGE U	UU	55	19b. TELEPHONE NUMBER *(include area code)*

Standard Form 298 (Rev. 8-98)
Prescribed by ANSI Std. Z39.18

Table of Contents

INTRODUCTION

The success of intensity-modulated radiation therapy (IMRT) or 4-D conformal radiation therapy (CRT) is heavily reliant on accurate image-guidance in prostate cancer treatment. Cone-beam CT (CBCT) image acquisition is becoming one of the dominant imaging modalities, and the accuracy of the images by CBCT and the radiation dose due to CBCT are considered as very important issues [1,2]. Most scanning geometries of the CBCT used in prostate cancer treatment are circular trajectories, which often yield insufficient data for exact volumetric image reconstruction. As a consequense, images reconstructed by approximate algorithms, mostly based on the Feldkamp algorithm, would contain image artifacts such as streaks, intensity drop, and image deformation in regions away from the trajectory plane [3]. Radiation dose to the prostate cancer patient due to CBCT must be carefully studied and imaging schemes that can lead to minimum (or optimum if interplay between imaging and therapeutic dose conformity is considered) dose should be devised. This is of paramount importance especially in repeated scans during the treatment process to adapt treatment plans to changes in prostate over time. The overall objective of this project is to investigate and develop innovative CBCT scanning methods and corresponding image reconstruction algorithms that can increase the accuracy of the images of the patient's prostate and/or reduce patient dose from CBCT. Reverse helical CBCT has been developed for exact reconstruction of volumetric images, region-of-interest (ROI) reconstruction methods have been explored to reduce patient dose, and a few-view CBCT approach has been proposed for enormous reduction of patient dose. This report summarizes the progress of this Predoctoral Traineeship Award project made by the recipient during the past one year.

<div align="center">BODY</div>

1 Training Accomplishments

At the time of this report, the recipient, Seungryong Cho, of the Predoctoral Traineeship Award has taken 22 out of 22 required courses towards his Ph.D. degree in medical physics. The courses include physics of medical imaging, physics of radiation therapy, mathematics for medical physicists, image guided radiation therapy, statistics, anatomy of the body, radiation biology and teaching assistantship.

2 Research Accomplishments

2.1 Investigation of reconstruction algorithms for reverse helical CBCT

Helical scanning configuration has been used widely in diagnostic CBCT for acquiring data sufficient for exact image reconstruction over an extended volume. In image-guided radiation therapy (IGRT) and other applications of CBCT, it is difficult, if not impossible, to implement mechanically a multiple-turn helical trajectory on the imaging systems due to hardware constraints. However, imaging systems in these applications often allow for the implementation of a reverse helical trajectory in which the rotation direction changes between two turns. Because the reverse helical trajectory satisfies Tuy's condition, it yields data sufficient for exact image reconstruction within the reverse helix volume. The recently developed chord-based algorithms such as the backprojection filtration (BPF) algorithm can readily be applied to reconstructing images on chords of a reverse helical trajectory, and they can thus reconstruct an image within a volume covered by the chords. Conversely, the chord-based algorithms cannot reconstruct images within regions that are not intersected by chords.

In a reverse helix volume, we have shown that chordless regions exist in which no images can thus be reconstructed by use of the chord-based algorithms. Therefore, we have recently developed a shift-invariant filtered backprojection (FBP) algorithm for exact image reconstruction within the reverse helix volume, including the chordless region. Results of the numerical studies confirm that the proposed FBP algorithm can exactly reconstruct an image within the entire reverse helix volume, including the chordless region. It is relatively straightforward to extend the proposed FBP algorithm to reconstruct images for general trajectories, including reverse helical trajectories with variable pitch, titled axis, and/or additional line segments between turns. The developed algorithm needs further investigation to handle a long object problem and thus to be applied to accurate image reconstruction of prostate, which is left as our future work. A full description of the algorithm is in reference [4] which is attached as Appendix A.

2.2 Investigation of ROI image reconstruction in circular CBCT

As an attempt to reduce patient dose, scanning time, and scatter to the detector , and also to increase the spatial resolution of the images from circular cone-beam data, we have investigated algorithms for ROI image reconstruction. A backprojection-filtration (BPF) algorithm based on PI-line concept has been developed to reconstruct ROI images from

truncated data set which contains only the projections of the ROI. Since a microCT system with a flat-panel detector shares the physics and scanning geometry of image acquisition with a CBCT system used in IGRT, we have built a prototype microCT that provides a hands-on experiment for validating new algorithms.

Using the microCT system, we have validated that the proposed BPF algorithm can reconstruct ROI images without any truncation artifacts which, in contrast, would exist in the images reconstructed by conventional algorithms. In microCT and also in CBCT of IGRT systems, because the detector size is limited, the use of a large geometric magnification can lead to truncated cone-beam data. Motivated by our results of ROI imaging, we proposed to exploit the unique capability of the BPF algorithm for accurate ROI image reconstruction from truncated data to improve spatial resolution of the ROI images of a mouse leg bearing osteosarcoma. The increased spatial resolution of the ROI images has been successfully demonstrated. Detailed work can be found in reference [5] which is also attached as Appendix B.

In most IGRT procedures, it is desirable to have accurate image of the target while sparing patient dose specifically to the normal tissue outside the target. This issue becomes more important in prostate cancer where there are radiation sensitive tissues near the treatment target such as rectum. Unfortunately, the ROI reconstructible by the chord-based algorithms cannot be exclusively the target in general. The ROI usually contains more than the target including those organs sensitive to the radiation. In this regard, we proposed an innovative, intensity-weighted ROI imaging technique to lower patient dose to the normal tissue surrounding the target and at the same time to preserve the image quality of the target in the ROI. The ROI in this task is divided into two subROI's. Higher dose is delivered to the inner ROI containing the target, and lower dose is to the outer ROI. Each projection image, therefore, will have different noise levels in two regions: inner ROI projection and outer ROI projection. This work is based on the observation that the noise from the outer ROI does not significantly propagate into the inner ROI due to noise transfer property of the Hilbert transform. The preliminary study has been submitted to SPIE Medical Imaging Conference, 2008 [6]. The abstract is attached as Appendix C.

2.3   Investigation of few-view CBCT for IGRT

The recently available kV cone-beam imaging capability of a linear accelerator system provides excellent soft-tissue contrast, which is an important benefit in IGRT of such as prostate cancer. Reduction of the treatment margins owing to improved image quality of the target would increase the conformality of dose distribution in a fractionated treatment where day-to-day, interfraction organ motion is present. However, radiation dose accumulated to the patient due to daily CBCT before each fractionated treatment may pose a challenge in the patient's radiation safety. This motivated our work to develop a few-view CBCT for IGRT, where few-view means a limited number of projection views out of 360° in a circular scan.

Recently, we have developed an iterative image reconstruction algorithm based on total-variation (TV) minimization from incomplete cone-beam projection data [7]. In numerical studies with a variety of incomplete cone-beam data sets including truncated data, reduced scan range, and sparse sampling, the developed algorithm, which is referred to as TV algorithm hereafter, showed an excellent performance compared with existing algorithms such as algebraic reconstruction technique (ART) and expectation maximization (EM). The TV

algorithm begins in general with a uniform image as an initial guess, and goes through iteration steps to minimize the image TV. In an IGRT of prostate cancer, a patient usually undergoes a CT scanning for treatment planning, which can provide the reference image for image-guidance procedure. Therefore, we proposed a TV algorithm with *a priori* information in few-view CBCT for IGRT. We expect the proposed algorithm can reduce the number of projections needed for volumetric image reconstruction even further than a TV algorithm without *a priori* information does. The number of projections needed in this approach would be less than that of conventional CBCT by factor of tens. The preliminary study has been submitted to SPIE Medical Imaging Conference, 2008 [8]. The abstract is also attached as Appendix D.

KEY RESEARCH ACCOMPLISHMENTS

- We have proposed a novel image acquisition geometry of reverse helix for CBCT imagers mounted on LINAC treatment systems used for prostate cancer IGRT, and developed an exact reconstruction algorithm of the volumetric images within the reverse helix.

- We have developed a prototype microCT with a flat-panel detector, which has common physics of image acquisition with CBCT imagers mounted on LINAC treatment systems, to experimentally validate newly developed algorithms for prostate cancer IGRT.

- We have conducted an ROI image reconstruction of a mouse having osteosarcoma on one leg. A larger geometric magnification has been attempted to increase the spatial resolution of the ROI image, and the developed BPF algorithm successfully reconstructed the ROI image without truncation artifacts. This strategy can be applied to prostate cancer IGRT with reduced imaging dose.

- We have proposed and conducted a preliminary investigation of the intensity-weighted ROI imaging for CBCT in prostate cancer IGRT. The proposed method can bring in useful outcomes in terms of dose management and image-guidance.

- We have performed a preliminary, numerical study of few-view CBCT for prostate cancer IGRT based on TV algorithm with *a priori* information. The success of the proposed method would reduce the patient dose due to prostate cancer imaging by factor of tens.

REPORTABLE OUTCOMES

Peer-reviewed Journal Articles

1. **S. Cho**, J. Bian, C. A. Pelizzari, C. -T. Chen, T. -C. He, and X. Pan: Region of interest image reconstruction in circular cone-beam microCT, Med. Phys., **34**, pp.4923-4933, 2007.

2. **S. Cho**, D. Xia, C. A. Pelizzari, and X. Pan: Exact reconstruction of volumetric images in reverse helical cone-beam CT, Med. Phys., (submitted), 2007.

3. **S. Cho**, E. Y. Sidky, J. Bian, and X. Pan: Dual-energy computed radiography based on estimated spectral properties of a specimen radiographic system, Nucl. Inst. Meth. A,(submitted), 2007.

4. D. Xia, **S. Cho**, and X. Pan: Image reconstruction for a reduced scan in circular sinusoidal cone-beam CT, IEEE Trans. Med. Imag., (submitted), 2007.

Conference Proceeding Articles

1. **S. Cho**, D. Xia, C. A. Pelizzari, and X. Pan: Cone-beam CT with a modified reverse helical trajectory for long object problem , Proc. MIC, M18-282, 2007.

2. D. Xia, **S. Cho**, and X. Pan: Reconstructibel volume for cone-beam CT with a reduced saddle trajectory , Proc. MIC, M04-5, 2007.

3. D. Xia, **S. Cho**, and X. Pan: Image noise properties in circular sinusoidal cone-beam CT , Proc. MIC, M13-285, 2007.

4. **S. Cho**, D. Xia, C. A. Pelizzari, and X. Pan: Exact image reconstruction in reverse helical cone-beam CT , Proc. Fully 3D Meeting, pp. 84-87, 2007.

Conference Presentations and Abstracts

1. **S. Cho**, D. Xia, C. A. Pelizzari, and X. Pan: Reverse helical cone-beam CT and its applications to image-guided radiation therapy , presented at RSNA Annual Meeting, 2007.

2. **S. Cho**, D. Xia, C. A. Pelizzari, and X. Pan: Exact image reconstruction in reverse helical cone-beam CT for radiation therapy , presented at AAPM Annual Meeting and at AAPM Midwest Chapter Meeting, 2007.

3. **S. Cho**, E. Pearson, D. Xia, C. A. Pelizzari, and X. Pan: Intensity-weighted region-of-interest imaging in cone-beam CT , accepted to SPIE Medical Imaging Conference, 2008.

4. **S. Cho**, E. Y. Sidky, C. A. Pelizzari, and X. Pan: Few-view cone-beam computed tomography for image-guided radiation therapy , accepted to SPIE Medical Imaging Conference, 2008.

Honors and Awards

- Student Trainee Award, IEEE Medical Imaging Conference, 2007

- Young Investigator Award (2nd place), AAPM Midwest Chapter Meeting, 2007

CONCLUSIONS

The recipient of the Predoctoral Traineeship Award has finished the required courses towards his Ph.D. degree. These trainings have proven useful for the recipient to achieve the proposed research goals.

During the first year, we have investigated innovative approaches in cone-beam CT for IGRT that can increase the accuracy of the reconstructed images and/or reduce radiation dose to the patient having prostate cancer. Reverse helical cone-beam CT has been fully explored in the context of prostate cancer IGRT and exact image reconstruction algorithms have been proposed. ROI imaging methods have been proposed and corresponding image reconstruction algorithms have been developed. The technique has been exploited further to provide intensity-weighted ROI images that can reduce patient dose even further. Few-view cone-beam CT with *a priori* information has been investigated and preliminary results have shown that the proposed method can potentially decrease the radiation dose by factor of tens.

Overall, we have achieved the goals for the first year and laid down a solid foundation for the research in the next two years. Our goals in the next two years include implementation of reverse helical CBCT to the real system, applying different scanning geometries in CBCT for exact image acquisition, development of intensity-weighted ROI imaging for the real system, and investigation of few-view cone-beam CT with *a priori* information in depth; all of these will be studied in the context of applications to prostate cancer IGRT.

REFERENCES

1. D. Verellen, M. D. Ridder, N. Linthout, K. Tournel, G. Soete, and G. Storme: Innovations in image-guided radiotherapy, Nature Reviews Cancer, **7**, pp. 949-960, 2007.

2. M. J. Murphy, J. Balter, S. Balter, J. A. BenComo, I. J. Das, S. B. Jiang, C. -M. Ma, G. H. Olivera, R. F. Rodebaugh, K. J. Ruchala, H. Shirato, and F. -F. Yin: The management of imaging dose during image-guided radiotherapy: Report of the AAPM Task Group 75 , Med. Phys., **34**, pp. 4041-4063, 2007.

3. Y. Zou, A. A. Zamyatin, B. S. Chiang, and M. D. Silver: Reduction of streak artifacts in circular cone beam CT using scanograms, Proc. MIC, M18-294, 2007

4. S. Cho, D. Xia, C. A. Pelizzari, and X. Pan: Exact reconstruction of volumetric images in reverse helical cone-beam CT, Med. Phys., (submitted), 2007.

5. S. Cho, J. Bian, C. A. Pelizzari, C. -T. Chen, T. -C. He, and X. Pan: Region of interest image reconstruction in circular cone-beam microCT, Med. Phys., **34**, pp.4923-4933, 2007.

6. S. Cho, E. Pearson, D. Xia, C. A. Pelizzari, and X. Pan: Intensity-weighted region-of-interest imaging in cone-beam CT , accepted to SPIE Medical Imaging Conference, 2008.

7. E. Y. Sidky, C. -M. Kao, and X. Pan: Accurate image reconstruction from few-views and limited-angle data in divergent-beam CT, J. X-ray Sci. Tech. **14,** pp. 119-139, 2006.

8. S. Cho, E. Y. Sidky, C. A. Pelizzari, and X. Pan: Few-view cone-beam computed tomography for image-guided radiation therapy , accepted to SPIE Medical Imaging Conference, 2008.

APPENDICES

- Appendix A: S. Cho, D. Xia, C. A. Pelizzari, and X. Pan: Exact reconstruction of volumetric images in reverse helical cone-beam CT, Med. Phys., (submitted), 2007.

- Appendix B: S. Cho, J. Bian, C. A. Pelizzari, C. -T. Chen, T. -C. He, and X. Pan: Region of interest image reconstruction in circular cone-beam microCT, Med. Phys., **34**, pp.4923-4933, 2007.

- Appendix C: S. Cho, E. Pearson, D. Xia, C. A. Pelizzari, and X. Pan: Intensity-weighted region-of-interest imaging in cone-beam CT , abstract accepted to SPIE Medical Imaging Conference, 2008.

- Appendix D: S. Cho, E. Y. Sidky, C. A. Pelizzari, and X. Pan: Few-view cone-beam computed tomography for image-guided radiation therapy , abstract accepted to SPIE Medical Imaging Conference, 2008.

Exact Reconstruction of Volumetric Images in Reverse Helical Cone-beam CT

[1,2]Seungryong Cho, [1]Dan Xia, [2]Charles A. Pelizzari, and [1]Xiaochuan Pan

[1]Department of Radiology, University of Chicago, Chicago, IL 60637

[2]Department of Radiation and Cellular Oncology, University of Chicago, Chicago, IL 60637

Abstract

Helical scanning configuration has been used widely in diagnostic cone-beam computed tomography (CBCT) for acquiring data sufficient for exact image reconstruction over an extended volume. In image-guided radiation therapy (IGRT) and other applications of CBCT, it is difficult, if not impossible, to implement mechanically a multiple-turn helical trajectory on the imaging systems due to hardware constraints. However, imaging systems in these applications often allow for the implementation of a reverse helical trajectory in which the rotation direction changes between two turns. Because the reverse helical trajectory satisfies Tuy's condition, it yields data sufficient for exact image reconstruction within the reverse helix volume. The recently developed chord-based algorithms such as the backprojection filtration (BPF) algorithm can readily be applied to reconstructing images on chords of a reverse helical trajectory, and they can thus reconstruct an image within a volume covered by the chords. Conversely, the chord-based algorithms cannot reconstruct images within regions that are not intersected by chords. In a reverse helix volume, as shown below, chordless regions exist in which no images can thus be reconstructed by use of the chord-based algorithms. In this work, based upon Pack-Noo's formula, we have developed a shift-invariant filtered backprojection (FBP) algorithm for exact image reconstruction within the reverse helix volume, including the chordless region. We have also conducted numerical studies to demonstrate the chordless region in a reverse helix volume and to validate the proposed FBP algorithm for image reconstruction within the chordless region. Results of the numerical studies confirm that the proposed FBP algorithm can exactly reconstruct an image within the entire reverse helix volume, including the chordless region. It is relatively straightforward to extend the proposed FBP algorithm to reconstruct images for general trajectories, including reverse helical trajectories with variable pitch, titled axis, and/or additional line segments between turns.

1 Introduction

Computed tomography (CT) is used widely as one of the leading imaging modalities in image-guided radiation therapy (IGRT). In the last few years, cone-beam CT (CBCT) with a KV-source that is mounted on the rotation gantry of a linear accelerator

1

(LINAC) treatment system has become commercially available [1, 2, 3]. Integrating such a KV-CT imaging component into the LINAC system allows the KV-imaging and MV-treatment processes share identical spatial, and temporal information about the treated patient. Currently, a KV-CT imaging scanner mounted on LINAC treatment system acquires cone-beam data by use of a scanning configuration in which the x-ray source and the detector move along a circular trajectory, largely because the mechanical implementation of a circular configuration is relatively easy. The FDK algorithm [4] and its variations have been proposed, and widely used in practice, for reconstructing approximate images from circular cone-beam data. However, due to data insufficiency, there may exist cone-beam image artifacts that include intensity drop, streak artifacts, and image deformation in reconstructed images [5, 6, 7]. The image artifacts would become more serious when a larger cone-angle is used for acquiring data.

Helical source trajectory has become a standard scanning configuration in diagnostic CT because it can collect cone-beam data sufficient for exact reconstruction of volume images. Diagnostic CT achieves an extended longitudinal coverage by use of the slip-ring technology, which allows the x-ray source and the detector to rotate multiple turns continuously in one direction, while the patient couch is translated at a constant speed along one direction, thus forming a multiple-turn helical source trajectory. The LINAC-mounted KV cone-beam CT, however, can rotate only one turn in one direction, and it must reverse the rotation direction after each turn, because the rotation gantry of LINAC treatment system rotates in such a way. Therefore, the LINAC-mounted KV cone-beam CT imager can achieve only a one-turn helical source trajectory without altering the couch motion mode. It is expected that certain IGRT applications based on cone-beam CT images may benefit from an extended volume coverage of the patient [8]. Therefore, it is desirable to achieve an extended longitudinal coverage beyond that of a one-turn helical trajectory. One natural way to extend the longitudinal coverage is that the couch is translated continuously along one direction while the LINAC gantry reverses its rotation direction after each turn, thus resulting in a multiple-turn reserve helical trajectory.

In this work, we investigate image reconstruction from cone-beam data acquired with reverse helical trajectories. We first apply the recently developed chord-based algorithms [9, 10] to reconstructing images because they are directly applicable to any general continuous trajectories including reverse helical trajectories. A chord is defined as a line segment connecting any two points on a continuous source trajectory; and

2

chord-based algorithms reconstruct volume images through reconstructing images on all of the chords that intersect with the volume. Because any selected volume enclosed by a conventional helical trajectory used in diagnostic CT is covered completely by chords [10, 11], chord-based algorithms can reconstruct images within the selected volume for a conventional helical trajectory.

As will be shown below, however, some portions of the reverse helix volume are not intersected by any chords, thus forming chordless regions in which images cannot be reconstructed by use of the chord-based algorithms. Therefore, the main focus of the work is to develop a new algorithm for exactly reconstructing images within the entire reverse helix volume. This new algorithm is derived from Pack-Noo's formula [12, 13], and thus it is a shift-invariant filtered backprojection (FBP) reconstruction algorithm. We have first conducted a study to analyze and demonstrate numerically the chordless region in a reverse helix volume that cannot be reconstructed by use of the chord-based algorithm. Additional numerical studies were conducted to validate the proposed FBP algorithm for image reconstruction within the chordless region. Results of the numerical studies confirm that, unlike the chord-based BPF algorithm that can yield only an incomplete volume image, the proposed FBP algorithm can exactly reconstruct an image within the reverse helix volume. It is relatively straightforward to extend the proposed FBP algorithm to reconstruct images for general trajectories, including reverse helical trajectories with variable pitch, titled axis, and/or additional line segments between turns.

2 A Reverse Helical Trajectory

The conventional helical and reverse helical trajectories can be specified by the rotation angle λ of the source. For comparison, we give below the mathematical expressions for the two trajectories in the coordinate system that is fixed on the imaged object. For a conventional helical trajectory $\vec{r}_0(\lambda)$, it can be expressed as

$$\vec{r}_0(\lambda) = (R\cos\lambda, R\sin\lambda, \frac{h}{2\pi}\lambda), \quad \lambda \in [\lambda_s, \lambda_e], \tag{1}$$

where R denotes the distance from the source to the rotation axis, h the helical pitch, and λ_s and λ_e the starting and ending angle of the helical trajectory. In Fig. 1a, we display a two-turn conventional helical trajectory specified by $\lambda \in [\lambda_s, \lambda_e] = [-2\pi, 2\pi]$.

<center>3</center>

In contrast, the reverse helical trajectory $\vec{r}_0(\lambda)$ can be written as

$$\vec{r}_0(\lambda) = (R\cos((-1)^n\lambda), R\sin((-1)^n\lambda), \frac{h}{2\pi}\lambda), \quad \lambda \in [\lambda_s, \lambda_e], \qquad (2)$$

where integer n indicates the nth turn, and it can be written in terms of a floor function "$\lfloor \ \rfloor$" as

$$n = \lfloor \frac{\lambda}{2\pi} \rfloor + 1. \qquad (3)$$

Without loss of generality, we have assumed that the turn with $n = 0$ in the reverse helical trajectory is a turn in the conventional helical trajectory. For example, as shown in Fig. 1, for a two-turn reverse helical trajectory specified by $\lambda \in [\lambda_s, \lambda_e] = [-2\pi, 2\pi]$, we have

$$\begin{aligned}
\vec{r}_0(\lambda) &= (R\cos\lambda, R\sin\lambda, \frac{h}{2\pi}\lambda), \quad \lambda \in [-2\pi, 0) \\
\vec{r}_0(\lambda) &= (R\cos(-\lambda), R\sin(-\lambda), \frac{h}{2\pi}\lambda), \quad \lambda \in [0, 2\pi].
\end{aligned} \qquad (4)$$

Let $f(\vec{r})$ be an object function with a support that is contained completely within the volume enclosed by a reverse helical trajectory. The cone-beam projection from the source point $\vec{r}_0(\lambda)$ can be written as

$$g(\lambda, \hat{\theta}) = \int_0^{\infty} dt f(\vec{r}_0(\lambda) + t\hat{\theta}), \qquad (5)$$

where $\hat{\theta}$ denotes the direction of x-ray transform of $f(\vec{r})$ from $\vec{r}_0(\lambda)$. It can be shown that the reverse helical trajectory satisfies Tuy's sufficient condition [14], and thus an exact image can be reconstructed from reverse-helix data. The task of image reconstruction is to recover $f(\vec{r})$ from the cone-beam projection data acquired with a reverse helical trajectory $\vec{r}_0(\lambda)$ specified in Eq. (2).

3 Chord-based Algorithm for Reverse Helical Trajectories

In the past several years, algorithms have been developed for image reconstruction on chords for continuous trajectories [9, 10, 15, 16]. A chord of a continuous trajectory is defined as a line segment connecting any two points on the trajectory. If a volume is covered completely by chords, the image within the volume can be obtained through reconstructing images on all of the chords by use of the chord-based
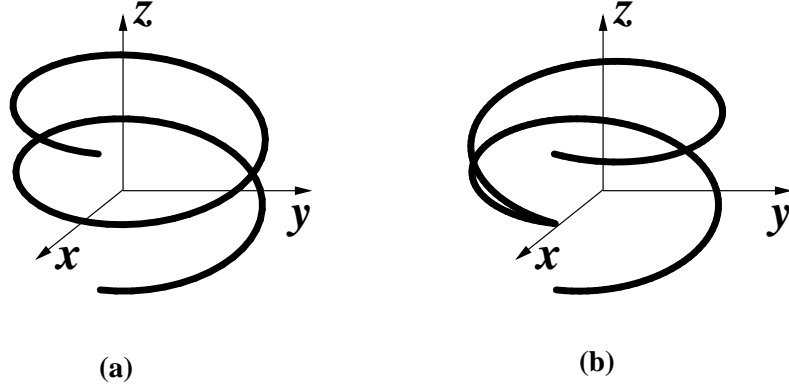
4

(a)   **(b)**

Figure 1: A two-turn conventional helical trajectory (a) and a two-turn reverse helical trajectory (b) in the coordinate system $\{x,y,z\}$ that is fixed on the imaged object.

algorithms. Although the chord-based algorithms can have the forms of backprojection filtration (BPF) [10, 15] and filtered backprojection (FBP) [16], we focus only on image reconstruction for a reverse helical trajectory by using the chord-based BPF algorithm in this section. Similar results can be obtained by use of the chord-based FBP algorithms.

3.1   Chord-based BPF algorithm

We consider a chord specified by λ_1 and λ_2 on a given source trajectory $\vec{r}_0(\lambda)$. Let

$$\hat{e}_c = \frac{\vec{r}_0(\lambda_2) - \vec{r}_0(\lambda_1)}{|\vec{r}_0(\lambda_2) - \vec{r}_0(\lambda_1)|} \tag{6}$$

denote the direction of the chord, as shown in Fig. 2. Also, we use x_c to indicate the coordinate of a point on the chord. It can be shown that the fixed coordinate and the chord coordinate of the point are related through

$$\vec{r} = \frac{1}{2}[\vec{r}_0(\lambda_1) + \vec{r}_0(\lambda_2)] + x_c\hat{e}_c, \quad x_c \in [-l, l], \tag{7}$$

where $l = \frac{1}{2}[\vec{r}_0(\lambda_2) - \vec{r}_0(\lambda_1)]$ denotes one half of the chord length.

Using $f_c(x_c, \lambda_1, \lambda_2)$ to denote the object function on the chord, we have

$$f(\vec{r}) = f_c(x_c, \lambda_1, \lambda_2), \tag{8}$$

where $\vec{r}$ and x_c are related through Eq. (7). Because the compact support of the object function is enclosed by the trajectory, the support of the object function on a chord is

5

finite. Without loss of generality, we assume that the object support on the chord is given by $x_c \in [x_{s1}, x_{s2}]$. Considering a segment $[x_{c1}, x_{c2}]$ on the chord that contains the support $x_c \in [x_{s1}, x_{s2}]$, i.e., $[x_{s1}, x_{s2}] \in [x_{c1}, x_{c2}]$, one has

$$f_c(x_c, \lambda_1, \lambda_2) = 0 \quad \text{for} \ \ x_c \notin [x_{s1}, x_{s2}]. \tag{9}$$

From cone-beam data $g(\lambda, \hat{\theta})$, one can compute a backprojection image onto the chord as

$$g_B(x_c, \lambda_1, \lambda_2) = \int_{\lambda_1}^{\lambda_2} \frac{d\lambda}{|\vec{r} - \vec{r}_0(\lambda)|} \left[\frac{\partial}{\partial \lambda} g(\lambda, \hat{\theta}) \right]_{\hat{\theta}}, \tag{10}$$

where $\vec{r}$ and x_c are related through Eq. (7). Based upon the backprojection image on the chord, the BPF algorithm reconstructs the object function $f_c(x_c, \lambda_1, \lambda_2)$ on the chord as

$$
\begin{aligned}
f_c(x_c, \lambda_1, \lambda_2) &= \frac{1}{2\pi^2} \frac{1}{\sqrt{(x_{c2} - x_c)(x_c - x_{c1})}} \\
&\times \ [\int_{x_{c1}}^{x_{c2}} \frac{dx'_c}{x_c - x'_c} \sqrt{(x_{c2} - x'_c)(x'_c - x_{c1})} \\
&\times \ g_B(x'_c, \lambda_1, \lambda_2) + C],
\end{aligned}
\tag{11}
$$

where $x_c \in [x_{c1}, x_{c2}]$, and the constant C is given by

$$C = 2\pi \int_{x_{c1}}^{x_{c2}} f_c(x_c, \lambda_1, \lambda_2) dx_c = 2\pi g(\lambda_1, \hat{e}_c). \tag{12}$$

3.2   Chord-based reconstructible volume

For a reverse helical trajectory, we define a one-turn trajectory segment as the portion in which the rotation direction of the source remains unchanged. The chords of a reverse helical trajectory can thus be divided into two classes: chords connecting two points within a one-turn trajectory segment, and chords connecting two points on two different one-turn trajectory segments, which we refer to as one-turn and multiple-turn chords, respectively. For a one-turn chord specified by λ_1 and λ_2, $|\lambda_1 - \lambda_2| \leq 2\pi$. Therefore, a one-turn chord of a reverse helical trajectory is equivalent to the PI-line segment in a conventional helical trajectory. We display in Figs. 3a and 3b one-turn and multiple-turn chords for a two-turn reverse helical trajectory.

It has been shown that each point enclosed by the conventional helical trajectory is intersected by at least one chord, and consequently that the volume enclosed can be
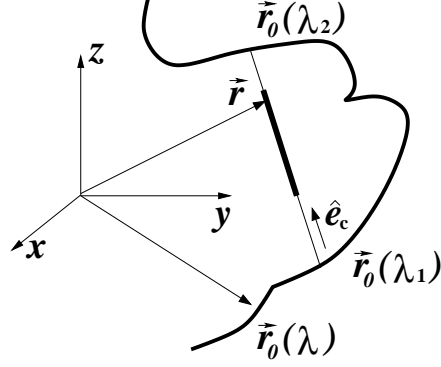
6

Figure 2: Illustration of a chord (thin line segment) specified by λ_1 and λ_2 for a general, continuous trajectory. The direction of a point on the chord is $\hat{e}_c$. The thick line segment on the chord indicates the support of the object.

covered completely by chords [11]. Therefore, the image within the volume enclosed by the conventional helical trajectory can be reconstructed through reconstructing images on chords intersecting with the volume. In a reverse helical trajectory with a finite number of turns, however, as shown in the appendix, region(s) exist that are not intersected by any chords, and thus image(s) within the region(s) cannot be reconstructed by use of the chord-based algorithms. For a given reverse helical trajectory, one can determine the reconstructible volume by use of the chord-based algorithm through computing the volume covered by the chords. In Fig. 4, we demonstrate the volumes covered by one-turn chords and multiple-turn chords for a two-turn reverse helical trajectory, which are the reconstructible volumes by use of the chord-based algorithms. Specifically, the white regions in Fig. 4 display the reconstructible areas by use of one-turn chords (a) and multiple-turn chords (b) on the sagittal (top row), coronal (middle row), and transverse (bottom row), respectively. Clearly, regions that are not covered by any chords exist for a two-turn reverse helical trajectory; and the use of multiple-turn chords can increase the reconstructible volume.

4   FBP Algorithm for a Reverse Helical Trajectory

In this section, using Pack-Noo's formula, we develop an FBP algorithm for image reconstruction from data acquired with a reversed helical trajectory.
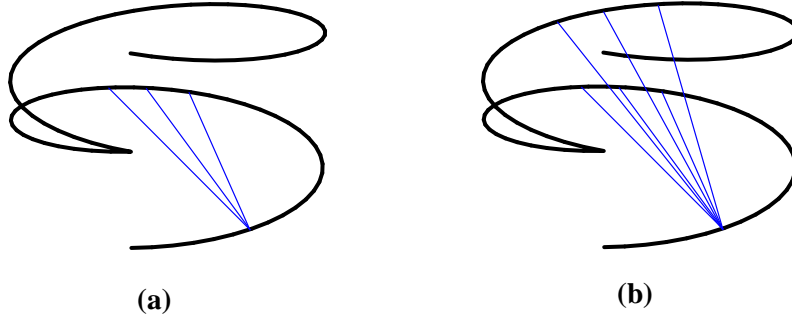
7

Figure 3: Illustration of chords (thin line segments) on a two-turn reverse helical trajectory (thick curve): one-turn chords (a), and multiple-turn chords (b).
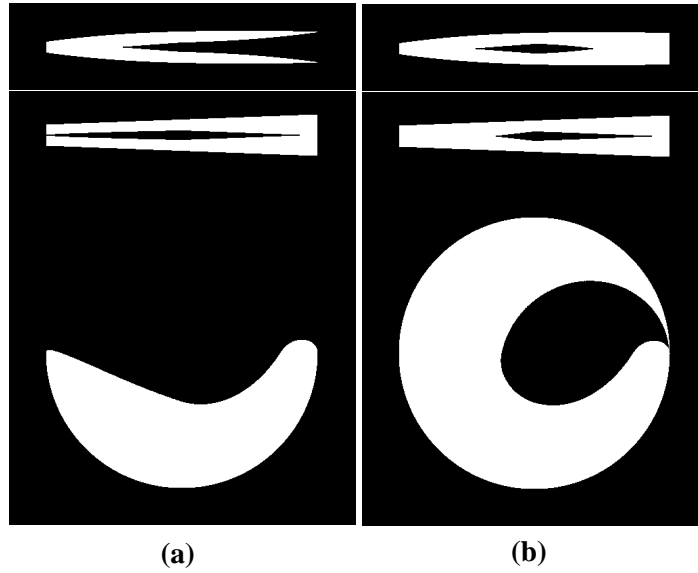

Figure 4: Regions (white) covered by one-turn chords (a) and two-turn chords (b) within slices specified by $x = 0$ (top row), $y = 0$ (middle row), and $z = 0$ (bottom row), respectively. Therefore, the white regions represent the reconstructible regions by use of the chord-based algorithms.

8

4.1 Pack-Noo's reconstruction formula

Pack-Noo's formula provides a basis for deriving FBP algorithms for image reconstruction for a general source trajectory [12, 17]. For a continuous segment of a trajectory $\vec{r}_0(\lambda)$ that begins and ends at λ^- and λ^+, we divide it into N adjacent, continuous subsegment trajectories of which the ith subsegment trajectory begins and ends at λ_i and λ_{i+1}, where $i = 1, 2, ...N$, $\lambda_1 = \lambda^-$, and $\lambda_{N+1} = \lambda^+$. Therefore, $[\lambda^-, \lambda^+] = [\lambda_1, \lambda_2] \cup [\lambda_2, \lambda_3] \cup \cdots [\lambda_i, \lambda_{i+1}] \cup \cdots [\lambda_N, \lambda_{N+1}]$. For each of the subsegment trajectories, Pack-Noo's formula provides a reconstruction as

$$\mathcal{K}(\vec{r}, \hat{e}_i, \lambda_i, \lambda_{i+1}) = -\frac{1}{2\pi^2} \int_{\lambda_i}^{\lambda_{i+1}} d\lambda \frac{1}{\|\vec{r} - \vec{r}_0(\lambda)\|} g_F(\lambda, \vec{r}, \hat{e}_i), \tag{13}$$

where $g_F(\lambda, \vec{r}, \hat{e}_i)$ represents the filtered backprojection data, given by

$$g_F(\lambda, \vec{r}, \hat{e}_i) = \int_{-\pi}^{\pi} d\gamma \frac{1}{\sin\gamma} \frac{\partial g(\lambda, \hat{\theta}(\lambda, \vec{r}, \hat{e}_i, \gamma))}{\partial \lambda}, \tag{14}$$

$$\hat{\theta}(\lambda, \vec{r}, \hat{e}_i, \gamma) = \cos\gamma \, \hat{\alpha}(\lambda, \vec{r}) + \sin\gamma \, \hat{\beta}(\lambda, \vec{r}, \hat{e}_i), \tag{15}$$

$$\hat{\beta}(\lambda, \vec{r}, \hat{e}_i) = \frac{\hat{e}_i - (\hat{e}_i \cdot \hat{\alpha}(\lambda, \vec{r}))\hat{\alpha}(\lambda, \vec{r})}{\|\hat{e}_i - (\hat{e}_i \cdot \hat{\alpha}(\lambda, \vec{r}))\hat{\alpha}(\lambda, \vec{r})\|}, \tag{16}$$

and

$$\hat{\alpha}(\lambda, \vec{r}) = \frac{\vec{r} - \vec{r}_0(\lambda)}{\|\vec{r} - \vec{r}_0(\lambda)\|}. \tag{17}$$

The integration over γ in Eq. (14) indicates a filtering process over the data derivative, while the filtering direction is determined by a preselected unit vector $\hat{e}_i \in S^2$ for a subsegment trajectory specified by $[\lambda_i, \lambda_{i+1}]$. As discussed below, the specific form of a derived FBP reconstruction algorithm depends critically upon an appropriate selection of $\hat{e}_i \in S^2$.

For a given subsegment trajectory $[\lambda_i, \lambda_{i+1}]$ and a selected unit vector $\hat{e}_i$, the reconstruction term $\mathcal{K}(\vec{r}, \hat{e}_i, \lambda^-, \lambda^+)$, as indicated in Eq. (13), can be computed from cone-beam projections and can thus be interpreted as the known data function. Let $(R''f)(\hat{\omega}, \vec{r} \cdot \hat{\omega})$ denote the second order derivative of the 3D Radon transform of the object function $f(\vec{r})$. Pack-Noo's formula [12] establishes a relationship between $\mathcal{K}(\vec{r}, \hat{e}_i, \lambda^-, \lambda^+)$ and $(R''f)(\hat{\omega}, \vec{r} \cdot \hat{\omega})$ as

$$\mathcal{K}(\vec{r}, \hat{e}_i, \lambda_i, \lambda_{i+1}) = -\frac{1}{8\pi^2} \int_{S^2} d\hat{\omega}(R''f)(\hat{\omega}, \vec{r} \cdot \hat{\omega})\sigma(\vec{r}, \hat{\omega}, \hat{e}_i, \lambda_i, \lambda_{i+1}), \tag{18}$$

9

where

$$\sigma(\vec{r}, \hat{\omega}, \hat{e}_i, \lambda_i, \lambda_{i+1}) = \frac{1}{2}\text{sgn}(\hat{\omega} \cdot \hat{e}_i)\left[\text{sgn}(\hat{\omega} \cdot \hat{\alpha}(\lambda_i, \vec{r})) - \text{sgn}(\hat{\omega} \cdot \hat{\alpha}(\lambda_i, \vec{r}))\right], \quad (19)$$

and "sgn" denotes the signum function. Therefore, for the N continuous subsegment trajectories covering the entire trajectory $\lambda \in [\lambda^-, \lambda^+]$, we have

$$\sum_{i=1}^{N} \mathcal{K}(\vec{r}, \hat{e}_i, \lambda_i, \lambda_{i+1}) = -\frac{1}{8\pi^2} \int_{S^2} d\hat{\omega}(R''f)(\hat{\omega}, \vec{r} \cdot \hat{\omega})\bar{\sigma}(\vec{r}, \hat{\omega}, \lambda_i, \lambda_{i+1}), \quad (20)$$

where

$$\bar{\sigma}(\vec{r}, \hat{\omega}, \lambda^-, \lambda^+) = \sum_{i=1}^{N} \sigma(\vec{r}, \hat{\omega}, \hat{e}_i, \lambda_i, \lambda_{i+1}). \quad (21)$$

It can be observed that, if the weighting function

$$\bar{\sigma}(\vec{r}, \hat{\omega}, \lambda^-, \lambda^+) = P = const., \quad (22)$$

the right-hand side of Eq. (20) yields exactly P-times the inverse 3D Radon transform of the object function. Under the condition in Eq. (22), the object function $f(\vec{r})$ is obtained as

$$f(\vec{x}) = \frac{1}{P} \sum_{i=1}^{N} \mathcal{K}(\vec{r}, \hat{e}_i, \lambda_i, \lambda_{i+1}). \quad (23)$$

The result in Eq. (23) is referred to as the FBP reconstruction algorithm, and its derivation, as discussed above, depends upon the appropriate selection of the unit vectors $\{\hat{e}_i\}$ for determining the filtering directions and upon the calculation of $\{\mathcal{K}(\vec{r}, \hat{e}_i, \lambda_i, \lambda_{i+1})\}$.

4.2   The FBP algorithm for reverse helical trajectories

Using Pack-Noo's formula, we derive below an FBP algorithm for image reconstruction from cone-beam data acquired with a two-turn reverse helical trajectory. Extension of the derived algorithm to multiple-turn reverse helical trajectories is straightforward and will be briefly described.

For a continuous scanning trajectory, one can define a polygon plane as the plane that intersects the trajectory at more than two points. For each side of a polygon, there exists a continuous subsegment of the source trajectory connecting two ends of the side of the polygon. Based on Pack-Noo's formula, a polygon-based FBP algorithm has been developed for image reconstruction for circular sinusoidal trajectories, including

10

the saddle trajectory [13]. For a circular sinusoidal trajectory, without loss of generality, we consider a polygon of 4 sides that intersects the trajectory 4 times. Let unit vectors $\hat{e}_i$ denote the directions of the polygon sides, i.e.,

$$\hat{e}_i = \frac{\vec{r}_0(\lambda_{i+1}) - \vec{r}_0(\lambda_i)}{\|\vec{r}_0(\lambda_{i+1}) - \vec{r}_0(\lambda_i)\|}, \tag{24}$$

where λ_i and λ_{i+1} denote the starting and ending points of the ith subsegment trajectory corresponding to the ith side of the polygon, and $i = 1, 2, 3,$ and 4. In this case, it has been shown [13, 18] that

$$\bar{\sigma}(\vec{r}, \hat{\omega}, \lambda^-, \lambda^+) = \sum_{i=1}^{4} \sigma(\vec{r}, \hat{\omega}, \hat{e}_i, \lambda_i, \lambda_{i+1}) = 2, \tag{25}$$

where $\lambda^- = \lambda_1$, $\lambda^+ = \lambda_5$, and $\vec{r}_0(\lambda^+) = \vec{r}_0(\lambda^-)$. Using this result in Eq. (23), one obtains the FBP algorithm for exact image reconstruction within the polygon, which is written as

$$f(\vec{r}) = \frac{1}{2} \sum_{i=1}^{4} \mathcal{K}(\vec{r}, \hat{e}_i, \lambda_i, \lambda_{i+1}). \tag{26}$$

We now extend the FBP algorithm above to reconstruct images for a two-turn reverse helical trajectory depicted in Fig. 5. First of all, it is important to observe, for a given point $\vec{r}$ within and the side direction $\hat{e}_i$ of the polygon, that both $\sigma(\vec{r}, \hat{\omega}, \hat{e}_i, \lambda_i, \lambda_{i+1})$ and $\mathcal{K}(\vec{r}, \hat{e}_i, \lambda_i, \lambda_{i+1})$ depend only upon the starting and ending points λ_i and λ_{i+1}, while being independent of the shape of the continuous subsegment trajectory corresponding to side i of the polygon. Therefore, the results in Eqs. (25) and (26) are directly applicable to image reconstruction within a 4-side polygon defined on a general trajectory, under the conditions that (1) $\lambda^- = \lambda_1$, $\lambda^+ = \lambda_5$, and $\vec{r}_0(\lambda^+) = \vec{r}_0(\lambda^-)$ and (2) each side of the polygon has a continuous subsegment trajectory connecting the two ends of the side.

Consider a polygon plane in Fig. 5a that is parallel to the y-z plane and that intersects the reverse helical trajectory at 4 distinctive points $\vec{r}_0(\lambda_i)$, where $i = 1, ..., 4$; and $-2\pi \leq \lambda_1 < \lambda_2... < \lambda_4 \leq 2\pi$. It can be observed in Fig. 5b that each of sides 1, 2, and 3 of the polygon has a distinct, continuous subsegment trajectory connecting its two ends. However, side 4 of the polygon has a distinct, discontinuous subsegment trajectory, which contains the starting and ending points λ_s and λ_e of the reverse helical trajectory, as displayed in Fig. 6a. Therefore, Eq. (26) cannot directly be applied to reconstructing an exact image within the polygon for the reverse helical trajectory.

11

A continuous subsegment trajectory for side 4 may be formed through including an additional continuous subsegment trajectory that connects the starting point λ_s and the ending point λ_e of the two-turn reverse helical trajectory. For example, a continuous subsegment trajectory passing λ_s and λ_e is formed in Fig. 6b, which includes an additional, straight subsegment trajectory connecting λ_s and λ_e. However, an additional subsegment trajectory requires an additional scan, thus resulting in additional scanning effort and radiation dose.

It is indeed possible to identify a continuous subsegment trajectory for side 4 without involving any additional scan to the reverse helical trajectory. As shown in Fig. 7, the union of the three distinct subsegment trajectories corresponding to sides 1, 2, and 3 of the polygon forms a continuous subsegment trajectory for side 4 of the polygon. As mentioned above, $\mathcal{K}(\vec{r}, \hat{e}_4, \lambda_4, \lambda_5)$ is independent of the shape of the continuous subsegment trajectory, while depending only upon λ_4 and λ_5, where λ_5 satisfies $\vec{r}_0(\lambda_5) = \vec{r}_0(\lambda_1)$. Therefore, we can use the union of three distinct subsegment trajectories of sides 1, 2, and 3 to compute $\mathcal{K}(\vec{r}, \hat{e}_4, \lambda_4, \lambda_5)$. In fact, from Eq. (5) and Eqs. (13-17), it can be seen that $\mathcal{K}(\vec{r}, \hat{e}_i, \lambda_i, \lambda_{i+1})$ depends upon λ_i and λ_{i+1} through $\vec{r}_0(\lambda_i)$ and $\vec{r}_0(\lambda_{i+1})$. Therefore,

$$\mathcal{K}(\vec{r}, \hat{e}_4, \lambda_4, \lambda_5) = \mathcal{K}(\vec{r}, \hat{e}_4, \lambda_4, \lambda_1), \tag{27}$$

in which we have used $\vec{r}_0(\lambda_5) = \vec{r}_0(\lambda_1)$. Furthermore, using Eq. (13), one can readily show that

$$\mathcal{K}(\vec{r}, \hat{e}_i, \lambda_4, \lambda_1) = -\mathcal{K}(\vec{r}, \hat{e}_i, \lambda_1, \lambda_4). \tag{28}$$

Finally, an exact image reconstruction within the polygon for a two-turn reverse helical trajectory can be obtained as

$$
\begin{aligned}
f(\vec{r}) &= \frac{1}{2} \sum_{i=1}^{4} \mathcal{K}(\vec{r}, \hat{e}_i, \lambda_i, \lambda_{i+1}) \\
&= \frac{1}{2} \sum_{i=1}^{3} \mathcal{K}(\vec{r}, \hat{e}_i, \lambda_i, \lambda_{i+1}) - \frac{1}{2} \mathcal{K}(\vec{r}, \hat{e}_4, \lambda_1, \lambda_4).
\end{aligned} \tag{29}
$$

We refer to Eq. (29) as the FBP algorithm for image reconstruction for a reverse helical trajectory. As shown in Fig. 8, the volume enclosed by a reverse helical trajectory can be decomposed into a set of polygons. Therefore, one can achieve a volume-image reconstruction for a reverse helical trajectory through reconstructing images within the set of polygons by use of the FBP algorithm described.
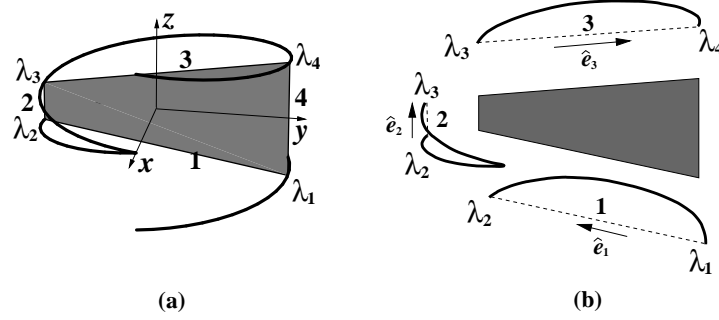
12

Figure 5: (a) The 4-side polygon (shaded region) formed by four chords each of which connects two points on the two-turn reverse helical trajectory. The polygon plane is chosen to be parallel to y-z plane. (b) Continuous subsegment trajectories (thick curves) corresponding to sides i of the 4-side polygon (dashed lines), and the directions $\hat{e}_i$ of the chords (i.e., the sides) of the polygon , where $i = 1, 2$, and 3.
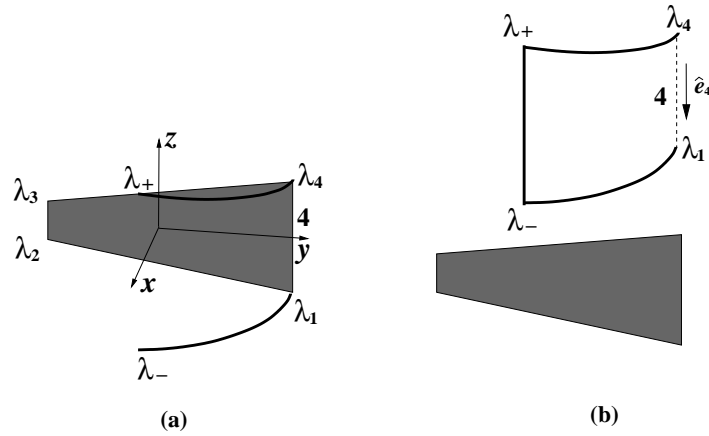

Figure 6: (a) For side 4 of the polygon (shade region), the subsegment trajectory containing the starting and ending points λ_s and λ_e consists of two discontinuous segments (thick curves). (b) A continuous subsegment trajectory passing λ_s and λ_e can be formed for side 4 through including, e.g., an additional, straight subsegment trajectory connecting λ_s and λ_e. Again, $\hat{e}_4$ denotes the direction of side 4 (dashed line) of the polygon.

13
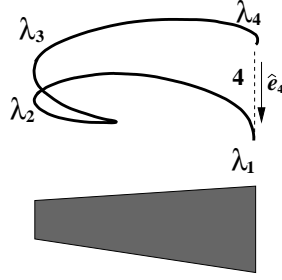
Figure 7: The portion of a two-turn reverse helical trajectory passing through λ_2 and λ_3 forms a continuous subsegment trajectory for side 4 of the polygon in Fig. 5.
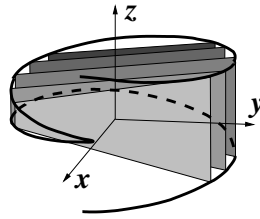
Figure 8: The volume enclosed by a two-turn reverse helical trajectory can be decomposed into a set of parallel polygons. Without loss of generality, a set of polygons parallel to y-z plane is shown. A volume image can be obtained through reconstructing images within the polygons by use of the proposed FBP algorithm.
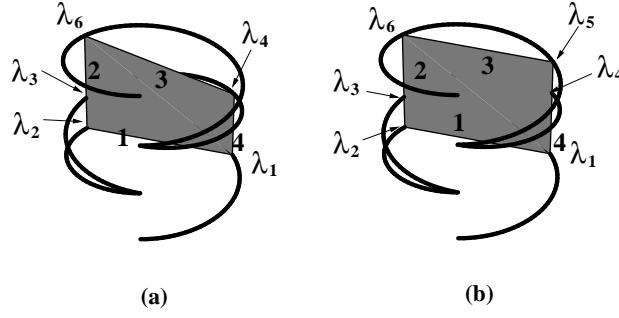
14

(a)   **(b)**

Figure 9: (a) A polygon with 4 corners intersecting the three-turn reverse helical trajectory at λ_1, λ_2, λ_4, and λ_6. (b) A polygon with 4 corners intersecting the three-turn reverse helical trajectory at λ_1, λ_2, λ_5, and λ_6.

The FBP algorithm above was derived for a two-turn reverse helical trajectory. Similar approach can readily be applied to deriving an FBP algorithm for multiple-turn reverse helical trajectories. Without loss of generality, we use a three-turn reverse helical trajectory to illustrate such an extension. Again, for the given reverse helical trajectory, we first select a 4-side polygon whose four corners reside on the trajectory, as shown in Fig. 9. In the case of a multiple-turn reverse helical trajectory, different polygons can be devised. In Figs. 9a and 9b, two different 4-side polygons are displayed. In these cases, it can be readily shown that, when unit vectors $\{\hat{e}_i\}$ are selected along each of the sides of the polygon, the result in Eq.(25) remains unchanged. Furthermore, a continuous subsegment trajectory can be identified for each side of the polygon. In Fig. 10, we display the continuous subsegment trajectories for each side of the polygon in Fig. 9b. From these continuous subsegment trajectories, one can compute $\mathcal{K}(\vec{r}, \hat{e}_i, \lambda_i, \lambda_{i+1})$ and use them in Eq. (29) to obtain the image within the polygon. Finally, one can obtain a volume image by reconstructing 2D images within a set of polygons in the volume enclosed by the reverse helical trajectories, as displayed in Fig. 11.

5 Numerical results

We have performed computer simulation studies to validate that the proposed FBP algorithm can reconstruct images within the volume enclosed by a reverse helical trajectory, including the chordless regions that cannot be reconstructed by use of the chord-based algorithm. The low contrast 3D Shepp-Logan phantom was used that has an el-
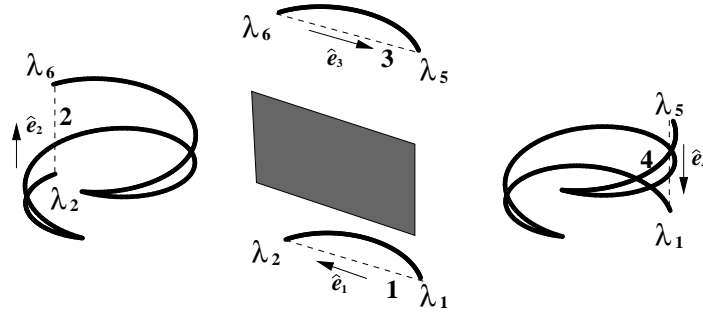
15

Figure 10: The continuous subsegment trajectories corresponding to each side side of the polygon in Fig. 9b.
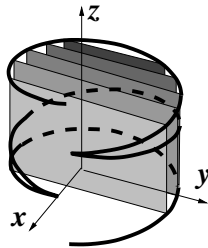

Figure 11: The volume enclosed by a three-turn reverse helical trajectory can be decomposed into a set of parallel polygons. A set of polygons parallel to y-z plane is shown here. A volume image can be obtained through reconstructing images within the polygons.

16

lipsoid support with axes of 13.8 cm, 18.0 cm, and 18.4 cm along the x-, y- and z-axis, respectively. The reverse helical trajectories have radii of $R = 60$ cm and the distances of $D = 75$ cm from the sources to detectors. For the purpose of clearly demonstrating the chordless region in the reconstruction, we used a helical pitch of $h = 15$ cm in the simulation study involving the chord-based BPF algorithm. We used helical pitch of $h = 40$ cm in the simulation study for the proposed FBP algorithm. The detector panel considered here has an effective square area that consists of 400×400 pixels each of which has a size of 0.78×0.78 mm^2.

In Figs. 12 and 13, we display images within slices at $x = 0$ cm (a), $y = 0$ cm (b), and $z = -2.5$ cm (c) reconstructed on one-turn and multiple-turn chords by using the chord-based BPF algorithm. Clearly, the BPF algorithm can accurately reconstruct images within the regions covered the chords. Comparison of the reconstructible regions in Figs. 12 and 13 indicates that the use of multiple-turn chords leads to a larger reconstructible region than that only from the one-turn chords. However, it can also be observed in both cases that the BPF algorithm cannot yield images within the chordless regions (e.g., the dark regions between the two reconstructible regions).

In Fig. 14, we show images within slices at $x = 0$ cm (a), $y = 0$ cm (b), and $z = -2.5$ cm (c) reconstructed by using the proposed FBP algorithm. The results indicate that the proposed algorithm can reconstruct an image within the volume enclosed by a reverse helical trajectory. In an attempt to demonstrate quantitatively the reconstruction accuracy, we display in Fig. 15a the profile along a vertical line, specified by $x = 0$ cm and $y = -2.5$ cm, passing through the Shepp-Logan phantom, as indicated in Fig. 15b. For comparison, we also plot the corresponding true profile as dotted curve in Fig. 15a. The profile results suggest that the proposed FBP algorithm can accurately reconstruct an image within the entire volume enclosed by the reverse helical trajectory. We have also performed a preliminary reconstruction from noisy data by use of the proposed FBP algorithm. We included Gaussian noise in the projection data with the noise level of 0.25 %. From the noisy data, we reconstructed images by use of the proposed FBP algorithm. In Fig. 16, we display the reconstructed noisy images within slices at $x = 0$ cm (a), $y = 0$ cm (b), and $z = -2.5$ cm (c).

6 Discussion

In the work, we have proposed reverse helical trajectories for acquiring cone-beam data, and have investigated and developed algorithms for image reconstruction from
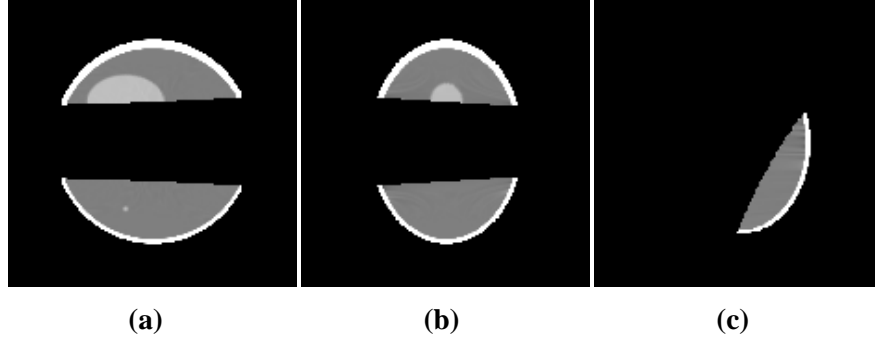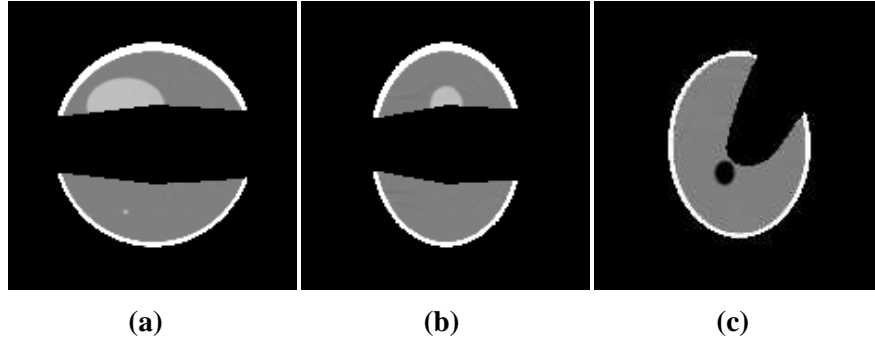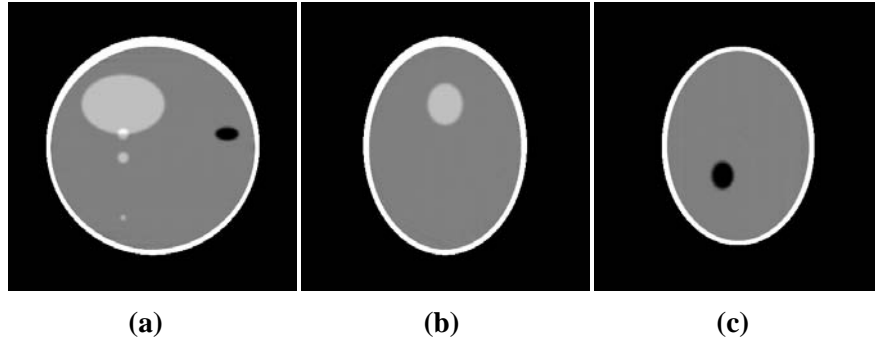
17

(a)　　　　　　　　**(b)**　　　　　　　　**(c)**

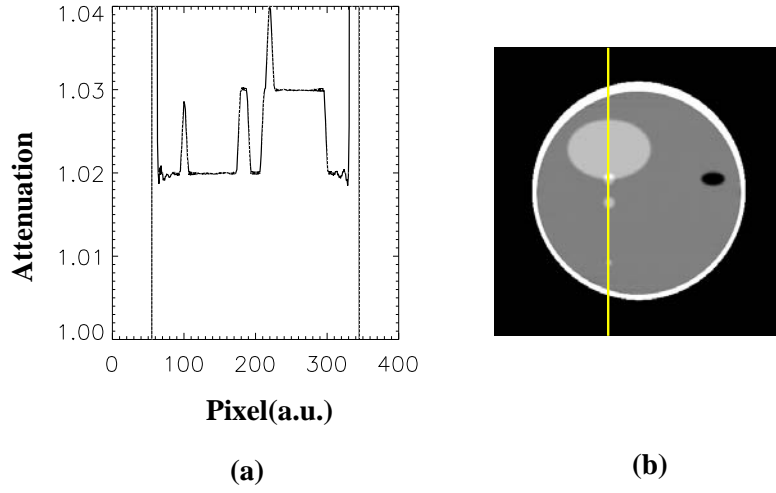Figure 12: Images within slices at $x = 0$ cm (a), $y = 0$ cm (b), and $z = -2.5$ cm (c) reconstructed from noiseless data by use of the chord-based algorithm on one-turn chords. The display window used in this paper is [1.0,1.04].

(a)　　　　　　　　**(b)**　　　　　　　　**(c)**

Figure 13: Images within slices at $x = 0$ cm (a), $y = 0$ cm (b), and $z = -2.5$ cm (c) reconstructed from noiseless data by use of the chord-based algorithm on both one-turn and two-turn chords.

(a)　　　　　　　　**(b)**　　　　　　　　**(c)**

Figure 14: Images within slices at $x = 0$ cm (a), $y = 0$ cm (b), and $z = -2.5$ cm (c) reconstructed from noiseless data by use of the proposed FBP algorithm.

18

Figure 15: (a) Profile on the vertical line specified by $x = 0$ cm and $y = -2.5$ cm, which is also indicated in (b). The reconstructed and true profiles are displayed as solid and dotted curves in (a).
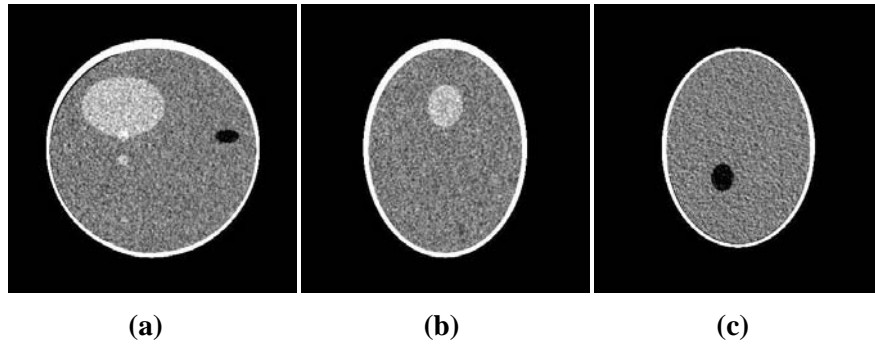

Figure 16: Images within slices at $x = 0$ cm (a), $y = 0$ cm (b), and $z = -2.5$ cm (c) reconstructed from the noisy data by use of the proposed FBP algorithm.

19

such cone-beam data. The proposed reverse helical trajectories and reconstruction algorithms may find IGRT and other applications. Recently, chord-based algorithms such as the BPF algorithm have been developed for image reconstruction from data acquired with general trajectories, provided that the trajectories not only satisfy Tuy's condition but also have chords covering their enclosed volumes. However, reverse helical trajectories are unique in that, although they satisfy Tuy's sufficient data condition, certain parts of the volume enclosed by them are not covered by chords. Consequently, the chord-based algorithms cannot reconstruct images within the chordless regions of reverse helical trajectories. For a given reverse helical trajectory, we have investigated its chordless regions; and we then conducted image reconstruction by use of the chord-based BPF algorithm to demonstrate the non-reconstructible, chordless regions.

As mentioned above, however, the volume enclosed by a reverse helical trajectory satisfies Tuy's condition, suggesting that an exact image within the reverse helix volume including the chordless regions can be reconstructed. We have proposed an FBP algorithm based on Pack-Noo's formula to reconstruct the images within the volume enclosed by a reverse helical trajectory, thus eliminating the chordless region that is non-reconstructible by use of the chord-based algorithms. Numerical studies were also conducted to validate the proposed FBP algorithm. Results of the numerical studies confirm that, unlike the chord-based algorithm, the proposed FBP algorithm can reconstruct an accurate image for the entire reverse helix volume. Interestingly, the developed FBP algorithm allows certain transverse data truncation. This is because the data filtering is determined only by the directions of the polygon sides within which the image is to be reconstructed. When the polygons covering the reverse helix volume are selected to be, e.g., parallel to the y-z plane, as we did here, data truncation along the x-axis outside the volume covered the polygons does not affect the image-reconstruction accuracy within these polygons. However, the proposed FBP algorithm generally allows no truncation longitudinally and is thus incapable of dealing with a long object problem. For a reverse helical trajectory with a long object problem, we are developing a combined image-reconstruction method in which the chord-based algorithm is used for addressing the long object problem, whereas the proposed FBP algorithm is used for dealing with image reconstruction within the chordless regions. The research of this combined method is beyond the scope of the current work and will be reported elsewhere in the future.

We have also discussed the extension of the proposed FBP algorithm to reconstruct

20

	λ_1	$-2\pi \leq \lambda_1 \leq -\pi$	$-\pi < \lambda_1 < 0$	$0 \leq \lambda_1 \leq \pi$	$\pi < \lambda_1 \leq 2\pi$
	$z(\lambda_1)$	$\frac{h}{2\pi}\lambda_1$	$\frac{h}{2\pi}\lambda_1$	$\frac{h}{2\pi}\lambda_1$	$\frac{h}{2\pi}\lambda_1$
One-turn chords	$z(\lambda_2)$	$\frac{h}{2\pi}(\lambda_1+\pi)$	none	$\frac{h}{2\pi}(\lambda_1+\pi)$	none
multiple-turn chords	$z(\lambda_2)$	$\frac{h}{2\pi}(-\lambda_1-\pi)$	$\frac{h}{2\pi}(-\lambda_1+\pi)$	none	none

Table 1: Relationship between the z-coordinates of chords passing through z-axis for a two-turn reverse helical trajectory.

images for multiple-turn reverse helical trajectories. In fact, it should be pointed out that the proposed FBP algorithm can readily be generalized to address the problems of image reconstruction for reverse helical trajectories with tilted axis, or variable pitches, or additional scanning trajectory segments.

7 Appendix: Analysis of the Chordless Regions in a Reverse Helical Trajectory

It is shown here that there exists chordless regions in the volume enclosed by a two-turn reverse helical trajectory. For simplifying the discussion, we consider intersecting points along z-axis, which is the rotation axis, with all the possible chords, and we show that there exists a region between intersecting regions on z-axis. A chord passing through z-axis defines a unique plane containing the chord and z-axis. For a given chord passing through z-axis, we label the angular parameter of the lower end by λ_1 and that of the upper end by λ_2. A chord for example is presented on the defined plane in Fig. 17. Using circular symmetry, we can establish the functional relationship, as summarized in Table 1, between $z(\lambda_1)$ and $z(\lambda_2)$ for one-turn chords and also for multiple-turn chords, where $z(\lambda)$ indicates the z-coordinate of a source point on the reverse helical trajectory at λ. The z-coordinate, $z_0(\lambda_1, \lambda_2)$, of the intersecting point of a chord with z-axis is given by

$$z_0(\lambda_1, \lambda_2) = \frac{1}{2}[z(\lambda_1) + z(\lambda_2)], \tag{30}$$

which is in the shaded regions in Fig. 17a and 17b for one-turn and multiple-turn chords. The chordless (white) region can be observed between the intersecting (shaded) regions.
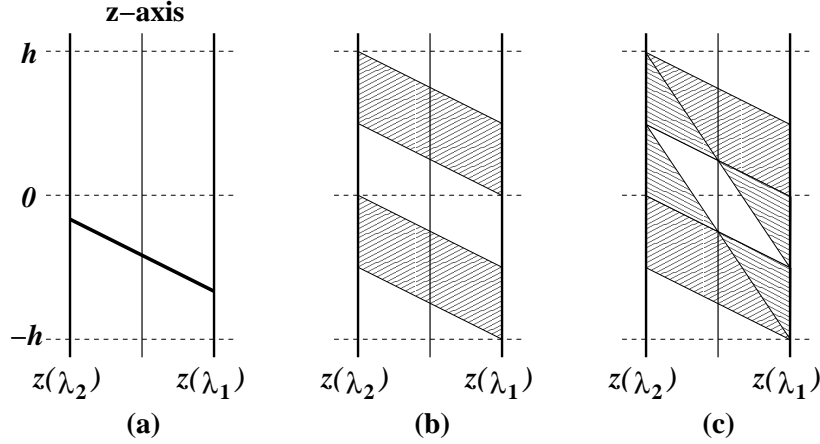
21

Figure 17: Diagrams demonstrating the chordless region along z-axis for a two-turn reverse helical trajectory. (a) An exemplary chord plotted on the plane defined by the chord and z-axis. (b) Collection of all one-turn chords. (c) Collection of all chords including multiple-turn chords.

8   Acknowledgments

References

[1] D. A. Jaffray and J. H. Siewerdsen, "Cone-beam computed tomography with a flat-panel imager: Initial performance characterization," *Med. Phys.*, vol. 27, pp. 1311–1323, 2000.

[2] J. H. Siewerdsen and D. A. Jaffray, "Optimization of x-ray imaging geometry (with specific application to flat-panel cone-beam computed tomography)," *Med. Phys.*, vol. 27, pp. 1903–1914, 2000.

[3] B. A. Groh, J. H. Siewerdsen, D. G. Drake, J. W. Wong, and D. A. Jaffray, "A performance comparison of flat-panel imager-based MV and kV cone-beam CT," *Med. Phys.*, vol. 29, pp. 967–975, 2002.

22

[4] L. A. Feldkamp, L. C. Davis, and J. W. Kress, "Practical cone-beam algorithm," *J. Opt. Soc. Am.*, vol. A1, pp. 612–619, 1984.

[5] S. Mori, M. Endo, S. Komatsu, S. Kandatsu, T. Yashiro, and M. Baba, "A combination-weighted Feldkamp-based reconstruction algorithm for cone-beam CT," *Phys. Med. Biol.*, vol. 51, pp. 3953–3965, 2006.

[6] S. Valton, F. Peyrin, and D. Sappey-Marinier, "Analysis of cone-beam artifacts in off-centered circular CT for four reconstruction methods," *Int. J. Biomed. Imag.*, vol. 2006, ID80421, pp. 1–8, 2006.

[7] Y. Zou, A. A. Zamyatin, B. S. Chiang, and M. D. Silver, "Reduction of streak artifacts in circular cone beam CT using scanograms," in *IEEE Medical Imaging Conference Record*, pp. M18–294, Honolulu, Hawaii, 2007.

[8] S. Yoo and F. Yin, "TU-FF-A2-01: Feasibility of cone-beam CT based treatment planning," *Med. Phys.*, vol. 33, p. 2219, 2006.

[9] Y. Zou, X. Pan, and E. Y. Sidky, "Theory and algorithms for image reconstruction on chords and within regions of interest," *Journal of the Optical Society of America*, vol. 22, pp. 2372–2384, 2005.

[10] Y. Zou and X. Pan, "Image reconstruction on PI-lines by use of filtered back-projection in helical cone-beam CT," *Phys. Med. Biol.*, vol. 49, pp. 2717–2731, 2004.

[11] P. E. Danielsson, P. Edholm, and M. Seger, "Towards exact 3D-reconstruction for helical cone-beam scanning of long objects. a new detector arrangement and a new completeness condition," in *Proceedings of the 1997 International Meeting on Fully Three-Dimensional Image Reconstruction in Radiology and Nuclear Medicine* (D. W. Townsend and P. E. Kinahan, eds.), pp. 141–144, Pittsburgh, 1997.

[12] J. D. Pack and F. Noo, "Cone-beam reconstruction using 1D filtering along the projection of M-lines," *Inv. Prob.*, vol. 21, pp. 1105–1120, 2005.

[13] H. Yang, M. Li, K. Koizumi, and H. Kudo, "Application of Pack and Noo's cone-beam inversion formula to a wide class of trajectories," in *IEEE Medical Imaging Conference Record*, pp. M14–450, San Diego, California, 2006.

23

[14] H. K. Tuy, "An inversion formula for cone-beam reconstruction," *SIAM J. Appl. Math.*, vol. 43, pp. 546–552, 1983.

[15] Y. Zou and X. Pan, "An extended data function and its backprojection onto PI-lines in helical cone-beam CT," *Phys. Med. Biol.*, vol. 49, pp. N383–N387, 2004.

[16] E. Y. Sidky, Y. Zou, and X. Pan, "Minimum data image reconstruction algorithms with shift-invariant filtering for helical, cone-beam CT," *Phys. Med. Biol.*, vol. 50, pp. 1643–1657, 2005.

[17] J. D. Pack and F. Noo, "Cone-beam reconstruction outside R-lines using the backprojection of 1-D filtered data," in *Proceedings of the 2005 International Meeting on Fully Three-Dimensional Image Reconstruction in Radiology and Nuclear Medicine*, pp. 287–290, Salt Lake City, Utah, 2005.

[18] H. Yang, M. Li, K. Koizumi, and H. Kudo, "Exact cone beam reconstruction for a saddle trajectory," *Phys. Med. Biol.*, vol. 51, pp. 1157–1172, 2006.

24

Region-of-interest image reconstruction in circular cone-beam microCT

Seungryong Cho
Department of Radiology and Department of Radiation and Cellular Oncology, University of Chicago, Chicago, Illinois 60637

Junguo Bian
Department of Radiology, University of Chicago, Chicago, Illinois 60637

Charles A. Pelizzari
Department of Radiation and Cellular Oncology, University of Chicago, Chicago, Illinois 60637

Chin-Tu Chen
Department of Radiology, University of Chicago, Chicago, Illinois 60637

Tong-Chuan He
Department of Surgery, University of Chicago, Chicago, Illinois 60637

Xiaochuan Pan[a)]
Department of Radiology, University of Chicago, Chicago, Illinois 60637

Cone-beam microcomputed tomography (microCT) is one of the most popular choices for small animal imaging which is becoming an important tool for studying animal models with transplanted diseases. Region-of-interest (ROI) imaging techniques in CT, which can reconstruct an ROI image from the projection data set of the ROI, can be used not only for reducing imaging-radiation exposure to the subject and scatters to the detector but also for potentially increasing spatial resolution of the reconstructed images. Increasing spatial resolution in microCT images can facilitate improved accuracy in many assessment tasks. A method proposed previously for increasing CT image spatial resolution entails the exploitation of the geometric magnification in cone-beam CT. Due to finite detector size, however, this method can lead to data truncation for a large geometric magnification. The Feldkamp-Davis-Kress (FDK) algorithm yields images with artifacts when truncated data are used, whereas the recently developed backprojection filtration (BPF) algorithm is capable of reconstructing ROI images without truncation artifacts from truncated cone-beam data. We apply the BPF algorithm to reconstructing ROI images from truncated data of three different objects acquired by our circular cone-beam microCT system. Reconstructed images by use of the FDK and BPF algorithms from both truncated and nontruncated cone-beam data are compared. The results of the experimental studies demonstrate that, from certain truncated data, the BPF algorithm can reconstruct ROI images with quality comparable to that reconstructed from nontruncated data. In contrast, the FDK algorithm yields ROI images with truncation artifacts. Therefore, an implication of the studies is that, when truncated data are acquired with a configuration of a large geometric magnification, the BPF algorithm can be used for effective enhancement of the spatial resolution of a ROI image. © *2007 American Association of Physicists in Medicine.* [DOI: 10.1118/1.2804924]

I. INTRODUCTION

With the rapid growth of both molecular probes for and animal models of human disease, small animal imaging is becoming an essential instrument in the investigator's toolbox. Microcomputed tomography (microCT) is particularly well suited for small animal imaging because of its high spatial resolution and high signal-to-noise ratio.[1–3] Applications of microCT imaging include the anatomic visualization of vascular structures (e.g., angiogenesis), tumors, bone pathology, and cardiac disease, with some microCT systems offering cardiac- and/or respiratory gating to improve resolution.[4–8] Indeed, high resolution microCT is often combined with functional imaging modalities such as single-photon emission computed tomography and positron emission tomography to coregister pathology to morphology.[9] Most microCT systems used in research include a charge coupled device or a flat panel detector as one of its main components, which leads to a cone-beam microCT scanning configuration.

In microCT applications, it is not uncommon that one seeks to obtain an image only within a region of interest (ROI) of the subject, and there remains active efforts in developing ROI imaging approaches, because they can lead to reduced imaging-radiation exposure to the subject and less data artifacts such as scatter. ROI imaging techniques can be roughly divided into two groups. One approach using the local tomography method provides edge-enhanced images from truncated data.[10] The local tomography can reconstruct singularities in tomographic images using the projection data only near each point in the ROI.[11] Even though the edge-enhanced images may be useful in imaging tasks where primary interest concerns the edge information,[12] this approach cannot improve image contrast information which is impor-

tant in most applications. An alternative approach, the so-called zoom-in method, utilizes two projection data sets; one obtained with a full field-of-view (FOV) scan and the other obtained with a limited FOV scan with a larger magnification.[13] A complete data set with locally varying sampling density, as a result, is prepared for image reconstruction, and high-resolution local imaging capability without contrast anomalies can be obtained. The major drawbacks of this approach, however, are doubled scan time and higher x-ray exposure, both of which are important issues in small animal imaging.

In recent years, considerable advances have been made in the development of analytic algorithms for image reconstruction in cone-beam CT. These algorithms have capabilities that cannot be achieved by conventional Feldkamp-Davis-Kress (FDK)-type algorithms.[14–17] For example, in a circular cone-beam CT which is the dominant scanning configuration for microCT animal imaging, the backprojection filtration (BPF) algorithm[18–20] can accurately reconstruct, from certain truncated projection data, ROI images free of truncation artifacts that would otherwise appear in the images reconstructed with the FDK-type algorithms. The PI-line-based BPF algorithm is an exact image reconstruction algorithm that reconstructs the image on the PI lines, the lines specifically defined for a helical cone-beam CT, by backprojecting the cone-beam data derivatives onto the PI lines and then by filtering along the PI lines. As discussed above, the zoom-in method requires, in addition to a limited FOV scan, a full FOV scan to avoid data truncation problem because it employs a FDK-type algorithm for image reconstruction. By use of the BPF algorithm, however, accurate ROI images without truncation artifacts can be obtained only from a single scan with a limited FOV.

The BPF algorithm for circular cone-beam CT has been used to reconstruct images from truncated cone-beam data for potential applications in image-guided radiation therapy.[21] Reduction of scanning time, one of the advantages of using ROI imaging with the PI-line-based BPF algorithm, has also been explored for reducing the amount of motion-contaminated data used for reconstruction in cardiac imaging.[22] In this work, we propose an ROI imaging approach, which exploits the useful features of the BPF algorithm for small animal imaging. Specifically, we apply the BPF algorithm to ROI imaging from truncated data of three different objects acquired with a circular cone-beam microCT system. We compare images reconstructed by use of the FDK and BPF algorithms from both truncated and nontruncated cone-beam data. The ROI images obtained with the BPF algorithm are virtually free of the truncation artifacts often observed in ROI images obtained with the FDK-type algorithms. It has previously been demonstrated quantitatively that image spatial resolution can be increased by use of data acquired with geometric magnification in convergent-beam CT.[23] In microCT, because the detector size is limited, the use of a large geometric magnification can lead to truncated data. Motivated by our results of ROI imaging, we also propose to exploit the unique capability of the BPF algorithm

for accurate ROI image reconstruction from truncated data to improve spatial resolution of the ROI image of a mouse leg bearing osteosarcoma.

The paper is organized as follows. In Sec. II, we summarize the ROI scanning configurations and the BPF algorithm. In Sec. III, we describe three phantoms and the microCT system used in our experimental studies. In Sec. IV, we perform validation studies using complete and truncated cone-beam data of the phantoms. Using the truncated data acquired with a large geometric magnification, we demonstrate the possibility of exploiting the unique property of the BPF algorithm for enhancing the spatial resolution of an ROI image. Finally, we discuss the implications of this research in Sec. V.

II. RECONSTRUCTION ALGORITHM

In this section, we describe the PI-line-based BPF algorithm for circular cone-beam CT, and describe the ROI scanning configuration used in this work.

II.A. PI-lines

The PI-line concept began to be used in research of image reconstruction for helical cone-beam CT, which has been a configuration of interest in diagnostic CT. A helical cone-beam scan can be obtained when the imaged object is translated longitudinally while the x-ray source and detector rotate on a transverse plane. From the perspective of the object, the source trajectory is a helix and can be written in the coordinate system $\{x, y, z\}$ that is fixed on the imaged object as

$$\mathbf{r}_0(\lambda) = \left(R \cos \lambda, R \sin \lambda, \frac{h}{2\pi}\lambda \right)^T, \tag{1}$$

where R denotes the distance from the source to the rotation axis, h the pitch of the helix, and λ the rotation angle of the x-ray source. A PI-line is defined as a straight line intersecting with the helical source trajectory at any two points labeled by λ_1 and λ_2, where $|\lambda_1 - \lambda_2| \leq 2\pi$.[24] Accordingly, a PI-line segment is defined as the line segment of a PI line inside the helix. It has been shown that a given point $\mathbf{r}$ within the helix determines a unique PI-line segment that passes through the point and also that all the possible PI-line segments can completely fill the space inside the helix.[24] Therefore, if the images on all the PI-line segments can be reconstructed, so can the object image inside the helix. As will be mathematically presented in the following sections, the PI-line-based BPF algorithm can exactly reconstruct the exact image on a PI-line segment from the projection data of the PI-line segment acquired from λ_1 to λ_2, where λ_1 and λ_2 define the PI-line segment of interest. The algorithm reconstructs the image on a PI-line segment by first backprojecting the data derivatives onto the PI-line segment and then performing a one-dimensional filtering along the PI line.
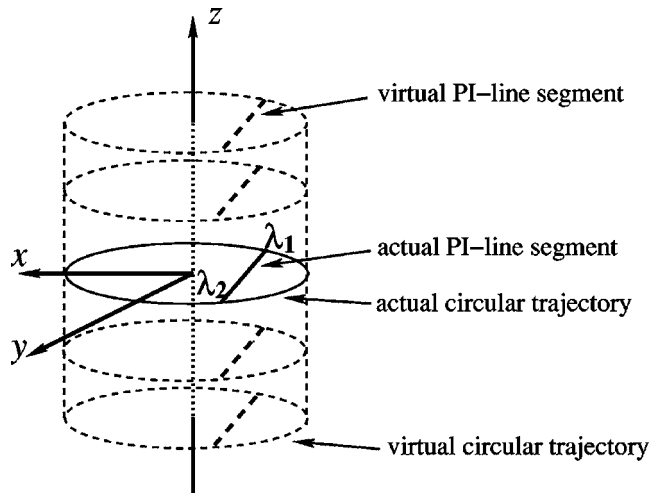
FIG. 1. Virtual circular trajectory and virtual PI-line segments. Actual PI-line segments are defined on the actual source trajectory at $z=0$ and virtual PI-line segments are defined similarly on virtual source trajectories at $z \neq 0$.

FIG. 2. (a) Cone-beam geometry with a circular source trajectory. The distance from the source to the center of the detector is represented by S. The center of rotation is represented by O which is the origin of the stationary coordinate $\{x,y,z\}$. The origin of the rotating coordinate $\{u,v,w\}$ is defined on the circular trajectory of radius R. $\{u_d, v_d\}$ is used as the detector coordinate. (b) A virtual PI-line segment connecting scanning angles specified by λ_1 and λ_2 at $z=z_0$ is parameterized by x_π.

II.B. Circular cone-beam scans and virtual PI lines

Since a circular trajectory can be considered as a helical trajectory with helical pitch of zero, the PI-line-based BPF algorithm can reconstruct the exact image of an object for the plane on which the physical source trajectory resides. We call this plane the midplane. Without loss of generality, the midplane can be represented by $z=0$, and the circular source trajectory can be expressed as

$$\mathbf{r}_c(\lambda) = (R \cos \lambda, R \sin \lambda, 0)^T. \tag{2}$$

An actual PI-line segment can be defined only within the midplane. For off midplanes (i.e., $z \neq 0$), no actual source trajectory and, consequently, no actual PI-line segment exists. Therefore, the PI-line-based BPF algorithm for helical cone-beam CT cannot be used directly for reconstructing images in off midplanes from cone-beam data. The concept of virtual trajectory and virtual PI-line segments has been introduced for approximate image reconstruction in off midplanes.[16]

As illustrated in Fig. 1, a virtual circular trajectory in an off midplane at $z \neq 0$ uses the z axis as its rotation axis and has a radius R identical to that of the actual circular trajectory in the midplane. The collection of the actual source trajectory and a stack of virtual circular trajectories encloses a three-dimensional (3D) cylindrical volume, which is referred to as the *virtual cylinder*. We define a straight line segment connecting any two points on a virtual trajectory as a virtual PI-line segment. It is not difficult to identify sets of actual PI-line segments that do not intersect with each other and thus that can fill completely the area enclosed by the actual circular trajectory.[16] Similarly, the virtual PI-line segments can be introduced to fill completely the area enclosed by a virtual circular trajectory. Therefore, the virtual cylinder can be completely filled by actual and virtual PI-line segments s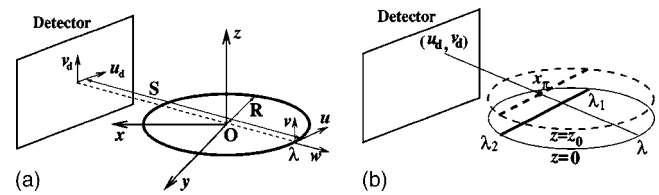o that the image of an object within the virtual cyl-inder can be reconstructed through reconstructing images on those PI-line segments.

II.C. BPF algorithm for circular cone-beam CT

For simplicity of discussion below, we will refer to both an actual and a virtual PI-line segment as a PI-line segment. We assume that the 3D image function $f(\mathbf{r})$ to be reconstructed situates entirely within the virtual cylinder. As shown in Fig. 2(a), two coordinate systems $\{x,y,z\}$ and $\{u,v,w\}$ are used to describe the geometry of a circular scan. They are fixed on the imaged object and the rotating source point, respectively, and referred to as the fixed-coordinate and the rotation-coordinate systems.

The unit vectors of the rotation-coordinate system are expressed in terms of the fixed-coordinate system as

$$\hat{e}_u(\lambda) = (-\sin \lambda, \cos \lambda, 0)^T,$$

$$\hat{e}_v(\lambda) = (0,0,1)^T, \tag{3}$$

$$\hat{e}_w(\lambda) = (\cos \lambda, \sin \lambda, 0)^T.$$

The fixed and rotation coordinates are related through

$$x = -u \sin \lambda + (w + R)\cos \lambda,$$

$$y = u \cos \lambda + (w + R)\sin \lambda,$$

$$z = v. \tag{4}$$

The planar detector located at a distance S from the source is oriented parallel to $\hat{e}_u$ and to $\hat{e}_v$ for all scanning angles λ as shown in Fig. 2(a). A point on the detector-coordinate (u_d, v_d) can be related to (u,v,w) in the rotation-coordinate system by

$$u_d = -\frac{S}{w}u, \quad v_d = -\frac{S}{w}v. \tag{5}$$

Cone-beam projections of the image $f(\mathbf{r})$ at a particular scanning angle λ and a detector position (u_d, v_d) can be expressed as

$$P(u_d, v_d, \lambda) = \int_0^\infty ds f[\mathbf{r}_c(\lambda) + s\hat{\beta}], \tag{6}$$

where $\hat{\beta}$ denotes the direction of the ray from the source to a specific detector position (u_d, v_d). $\hat{\beta}$ can be determined by

$$\hat{\beta} = \frac{1}{A(u_d, v_d)}[u_d \hat{e}_u(\lambda) + v_d \hat{e}_v(\lambda) - S\hat{e}_w(\lambda)], \tag{7}$$

where

$$A(u_d, v_d) = \sqrt{u_d^2 + v_d^2 + S^2}. \tag{8}$$

The direction of a PI-line segment is defined as

$$\hat{e}_{\pi c} = \frac{\mathbf{r}_c(\lambda_2) - \mathbf{r}_c(\lambda_1)}{|\mathbf{r}_c(\lambda_2) - \mathbf{r}_c(\lambda_1)|}. \tag{9}$$

The location of a point on a PI-line segment can be expressed as

$$\mathbf{r} = \mathbf{r}_{c1} + x_\pi \hat{e}_{\pi c}, \tag{10}$$

where

$$\mathbf{r}_{c1} = \frac{\mathbf{r}_c(\lambda_2) + \mathbf{r}_c(\lambda_1)}{2} + z_0 \hat{e}_v \tag{11}$$

and $x_\pi \in [x_{\pi 1}, x_{\pi 2}]$. The parameters, $x_{\pi 1}$ and $x_{\pi 2}$, denote the two ends of the PI-line segment. Therefore, a point $\mathbf{r}$ can be specified in terms of PI-line coordinates $\{x_\pi, \lambda_1, \lambda_2, z_0\}$ as shown in Fig. 2(b).

Let $f_\pi(x_\pi, \lambda_1, \lambda_2, z_0)$ denote the image on a PI-line segment. Also, let $x_{\pi \lambda 1}$ and $x_{\pi \lambda 2}$ denote the two ends of a support on the segment, whereby $f_\pi(x_\pi, \lambda_1, \lambda_2, z_0) = 0$ for $x_\pi \notin [x_{\pi \lambda 1}, x_{\pi \lambda 2}]$. We define the segment corresponding to $[x_{\pi \lambda 1}, x_{\pi \lambda 2}]$ as a PI-line *support segment*. By the assumption of the support size of $f(\mathbf{r})$, we have $[x_{\pi \lambda 1}, x_{\pi \lambda 2}] \subseteq [x_{\pi 1}, x_{\pi 2}]$. We also assume that the actual support of the object function on the PI-line is shorter than the support segment. The BPF algorithm for cone-beam scans can be written as follows:[20,21]

$$f_\pi(x_\pi, \lambda_1, \lambda_2, z_0) = \frac{1}{2\pi^2} \frac{1}{\sqrt{(x_{\pi \lambda 2} - x_\pi)(x_\pi - x_{\pi \lambda 1})}}$$
$$\times \left[\int_{x_{\pi \lambda 1}}^{x_{\pi \lambda 2}} dx_\pi' \frac{\sqrt{(x_{\pi \lambda 2} - x_\pi')(x_\pi' - x_{\pi \lambda 1})}}{(x_\pi - x_\pi')} \right.$$
$$\left. \times g_\pi(x_\pi', \lambda_1, \lambda_2, z_0) + 2\pi P_0 \right], \tag{12}$$

where $x_\pi \in [x_{\pi \lambda 1}, x_{\pi \lambda 2}]$ and P_0 is the projection along the ray coinciding with the PI-line segment. The backprojection term $g_\pi(x_\pi', \lambda_1, \lambda_2, z_0)$ can be expressed as

$$g_\pi(x_\pi', \lambda_1, \lambda_2, z_0) = \int_{\lambda_1}^{\lambda_2} \frac{d\lambda}{|\mathbf{r}' - \mathbf{r}_c(\lambda)|} \frac{d}{d\lambda} P(u_d', v_d', \lambda)|_{\hat{\beta}'}, \tag{13}$$

where $\mathbf{r}$ can be determined through Eq. (10) and (u_d', v_d') can be determined by Eqs. (4) and (5).

Note that the length of a PI-line support segment can be substantially smaller than the full length of the corresponding PI-line segment. The integration range in Eq. (12), which
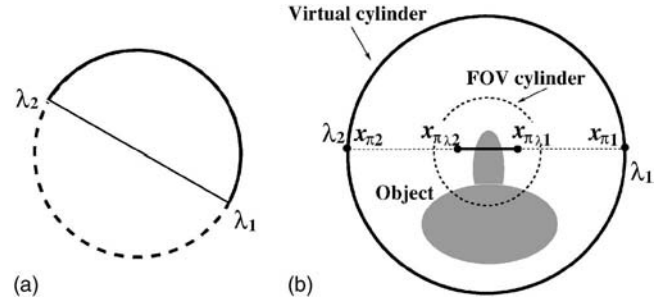

FIG. 3. (a) Redundancy in a full circular scan. Image on the PI-line segment connecting two scanning angles of λ_1 and λ_2 can be reconstructed using the data either from solid line part of the source trajectory or from dashed line part, or using the data from both parts. (b) Illustration of the ROI image reconstruction on a PI-line support segment. The FOV cylinder is determined by the fan angle of the cone beam. The length of a PI-line support segment, which is determined by $x_{\pi \lambda 1}$ and $x_{\pi \lambda 2}$, can be selected so as to cover the imaging target and to be completely enclosed by the FOV cylinder; $x_{\pi 1}$ and $x_{\pi 2}$ denote two end points of the PI-line segment.

is related to the filtering process, implies that the data backprojected only onto the PI-line support segment is needed to reconstruct the image on the corresponding PI-line segment. This is the key feature of the PI-line-based BPF algorithm that enables the ROI image reconstruction in this work.

II.D. ROI scanning configuration

Two data sufficiency conditions for reconstructing an image on a PI-line segment have been identified.[20,25] The first condition is that the angular reconstruction interval must be sufficient to reconstruct the image on the PI-line segment specified by λ_1 and λ_2. The second condition is that the illumination of the cone beam must be sufficient to cover the PI-line support segment, which is defined as $[x_{\pi \lambda 1}, x_{\pi \lambda 2}]$, at each projection view within the reconstruction interval. These data sufficiency conditions lead to a unique property of the PI-line-based BPF algorithm: It can reconstruct ROI images, from circular cone-beam data containing transverse truncation, with an accuracy comparable to that obtained from nontruncated circular cone-beam data.

In this work, a full scan, the range of which is 2π, has been used. The first condition of the data sufficiency conditions, therefore, is always satisfied and in fact there is a redundancy in the projection data for any PI-line segment. As shown in Fig. 3(a), the image on a PI-line segment specified by λ_1 and λ_2 can be reconstructed from two sets of conebeam data; one set comes from the scanning range depicted as a solid line, and the other from the dotted-lined part. We used $1/2$ as the weighting factor for the images reconstructed from two data sets.

The fan angle of the cone-beam has been fixed for every projection view to yield a constant FOV. The region under illumination for every projection view, therefore, in 3D constructs a cylindrical volume whose axis coincides with that of the virtual cylinder and whose radius, determined by the fan angle, is less than the radius of the virtual cylinder. We refer to this cylinder as an *FOV cylinder*. Note that the virtual cylinder is defined by the actual and virtual source tra-
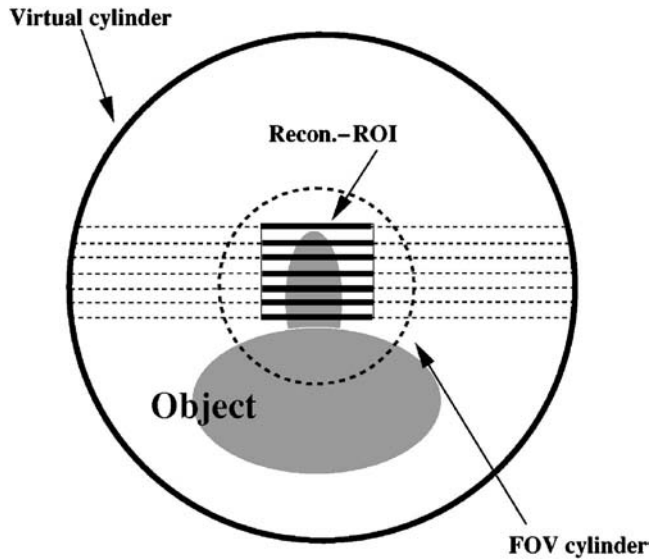
FIG. 4. Reconstructed ROI in this work. PI-line support segments are selected such that the set of them can form a rectangle covering the imaging target and being enclosed completely by the FOV cylinder. The PI-line segments are represented by dotted lines and corresponding PI-line support segments are represented by thick solid lines.

jectories, and the FOV cylinder is defined by the fixed fan angle of the cone-beam x ray. Schematic is shown in Fig. 3(b). Projection data outside of the FOV for each view have been truncated for ROI image reconstruction. The reconstructible ROI is now determined by the PI-line support segments within the FOV cylinder. For a PI-line segment specified by λ_1 and λ_2, as shown in Fig. 3(b), if the PI-line support segment, $[x_{\pi\lambda1}, x_{\pi\lambda2}]$, is completely located within the FOV cylinder, the image on the PI-line support segment can be reconstructed. In other words, the PI-line support segments can be selected such that they enclose the ROI object entirely and they are placed within the FOV cylinder. The PI-line support segments are selected in this work such that they
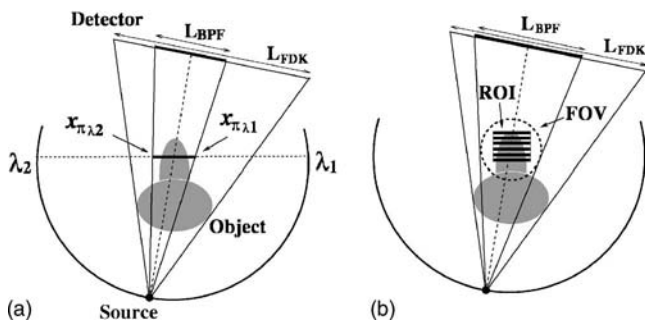

FIG. 5. Data requirements for the BPF algorithm and for the FDK algorithm. (a) For image reconstruction of points on a PI-line support segment defined by $x_{\pi\lambda1}$ and $x_{\pi\lambda2}$, at a given view, the BPF algorithm needs the data only of the projection only on the detector of the support segment, whereas the FDK algorithm requires full coverage of the object. Therefore, the detector sizes needed for the two algorithms are L_{BPF} and L_{FDK}, respectively. (b) For the scanning geometry of our work, as illustrated in Fig. 4, the BPF algorithm needs the projection data only within the length, L_{BPF}, of the detector for every view. In contrast, the FDK algorithm would need more projection data for every view than does the BPF algorithm.

form a rectangular ROI containing the target image as shown in Fig. 4.

In Fig. 5, the PI-line-based BPF algorithm used for ROI image reconstruction is conceptually compared with the FDK algorithm. In the FDK algorithm, since filtering process takes place before backprojection, the calculation of the filtering occurs on the detector plane and, as a result, the data required for exact image reconstruction of an ROI image must have no data truncation. Otherwise, the filtering process, when applied on truncated data, produces the truncation artifacts in the reconstructed images.[26] However, in the BPF algorithm, since the backprojection of the data derivative is filtered along each PI-line support segment, the calculation of the filtering occurs in the image space and, as a result, the data needed for exact image reconstruction of an ROI can be substantially smaller than that needed for the FDK algorithm. Specifically, at each view, the data only over the projection on the detector of a PI-line support segment are required for exact image reconstruction of the object on the PI-line support segment as shown in Fig. 5(a). As long as the image support on a PI line is covered completely by the PI-line support segment, filtering along the PI-line support segment after backprojection will not cause any artifacts. In this work, the ROI formed by the PI-line support segments is enclosed completely by the FOV cylinder defined by a constant size of detector as shown in Fig. 5(b). Therefore, although the data are truncated with respect to the entire object, they are sufficient for exact reconstruction of ROI images by use of the BPF algorithm.

Even though we have fixed the fan angle of the cone-beam in this work for the simplicity of the system, the fan angle can vary for each projection view such that only the set of PI-line support segments of the ROI is completely illuminated. Dynamically variable collimator can be devised and implemented for this purpose, and is planned for the future work.

III. SYSTEM AND PHANTOMS

We have applied the PI-line-based BPF algorithm to reconstructing ROI images of a physical phantom and mice from experimentally acquired cone-beam data.

III.A. MicroCT system

A prototype microCT system has been developed and its initial performance has been demonstrated.[27] The system consists of a microfocal x-ray source, an orthogonally mounted rotary stage with object holder, and a CsI-coupled complementary metal oxide semiconductor (CMOS) detector. The microfocal x-ray source (MX-20, Faxitron, USA), consisting of a tungsten anode with beryllium exit window, can be operated at between 10 and 35 kV, and can yield focal spot size of 20 μm. The 14 bit digital camera (Bioptics, USA) consists of a CsI scintillator plate and a 2048 $\times$ 1024 array of CMOS thin-film transistors and photodiodes. The length of the detector is 10.04 cm and the height is 5.02 cm. The rotation axis is aligned along the height direction of the detector. The rotary stage (ADRS-150, Aero-
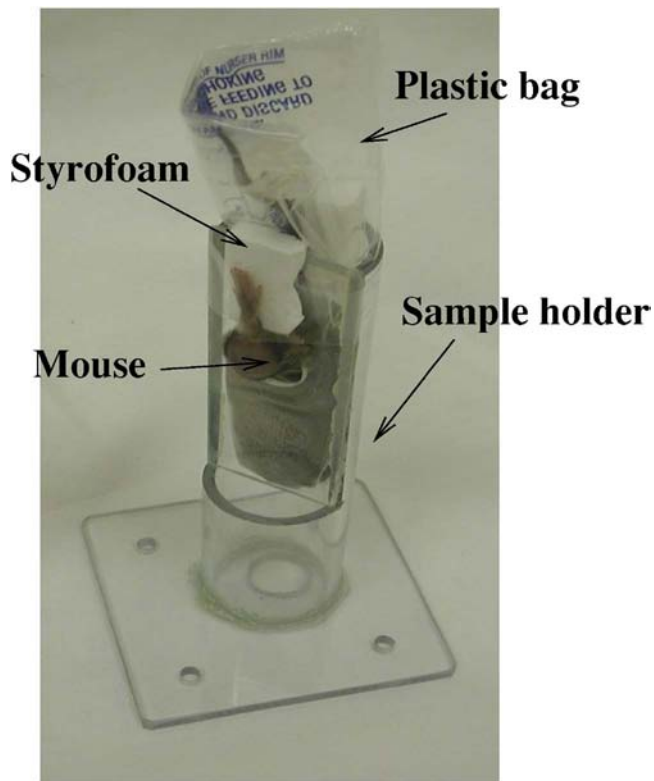
FIG. 6. Picture of a mouse in the sample holder. A formalin-fixed mouse is wrapped by a plastic bag and then tightly inserted to the sample holder through the hole of which the leg under interest is pulled out. A styrofoam is used to support the leg by taping.

tech, USA) has an accuracy about 10 arcsec. A robust and simple geometric calibration method has been devised and used to produce calibrated cone-beam data for image reconstruction.[26,27]

III.B. Materials

Three subjects were prepared for ROI imaging. The first is a uniform lucite phantom. Two circular cylinders with different diameters are put together and aligned along the rotation axis of the system. The diameter of the larger cylinder is 2 cm and that of the smaller one is 1 cm. The smaller cylinder is used as a ROI imaging target. The second is a formalin-fixed C3H mouse on one leg of which an FSa fibrosarcoma has been grown. The leg bearing the fibrosarcoma is considered as the ROI target. These two objects are used

for the purpose of validating practical applicability of the proposed algorithm. The validation in this work is not intended to evaluate thoroughly the algorithm itself, which has been done with numerical studies in our previous work,[20,21] but to demonstrate the ability of the algorithm to reconstruct ROI images experimentally. Graphical comparison study with line profiling of the reconstructed images will be performed for the validation. The third subject is another formalin-fixed mouse one leg of which contains an osteosarcoma. The leg bearing the osteosarcoma is again considered as the ROI target. Enhancement of the spatial resolution will be graphically presented using the reconstructed image of the osteosarcoma by the proposed algorithm.

A sample holder has been used to support the mice with the leg of interest placed at the rotation center as shown in Fig. 6. In order to help understand the imaging objects, we present 3D images reconstructed from complete data sets. Figure 7 shows volume-rendered views computed with opacity-weighted compositing and gradient-based shading (VolView 2.0: Kitware, Inc.) of the three objects reconstructed by the FDK algorithm from nontruncated data. Note that we have cropped the 3D reconstructed data so that we can remove some part of the sample holder to help visualize both the mouse body inside the sample holder and the leg outside of the sample holder.

IV. EXPERIMENTAL STUDIES

In this section, images reconstructed by use of the FDK algorithm and by the PI-line-based BPF algorithm from both truncated and nontruncated cone-beam data are systematically compared. It is important to understand that the validation of the proposed algorithm does not include correction schemes such as scatter correction and beam-hardening correction which may be necessary for obtaining more accurate images. The point is to compare the performance of the proposed algorithm with that of a conventional FDK algorithm in case of data truncation as well as of complete data.

IV.A. Lucite phantom studies

The full-scan projection data set were acquired at the radius of 37.1 cm for the circular trajectory and at 57.2 cm source-to-detector distance. Three hundred and sixty projection views spaced by 1° were obtained. The acquired data were then processed to reconstruct either full or ROI images of the phantom by use of a FDK algorithm and also by the
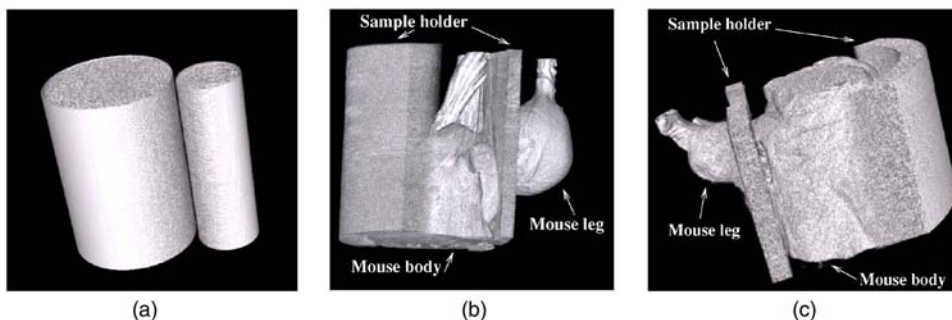

FIG. 7. Volume rendered images of the objects used in the work. (a) Lucite phantom. The smaller cylinder is considered as a ROI in this study. (b) A formalin-fixed mouse with one of its leg bearing FSa fibrosarcoma. (c) A formalin-fixed mouse with one of its leg bearing osteosarcoma.
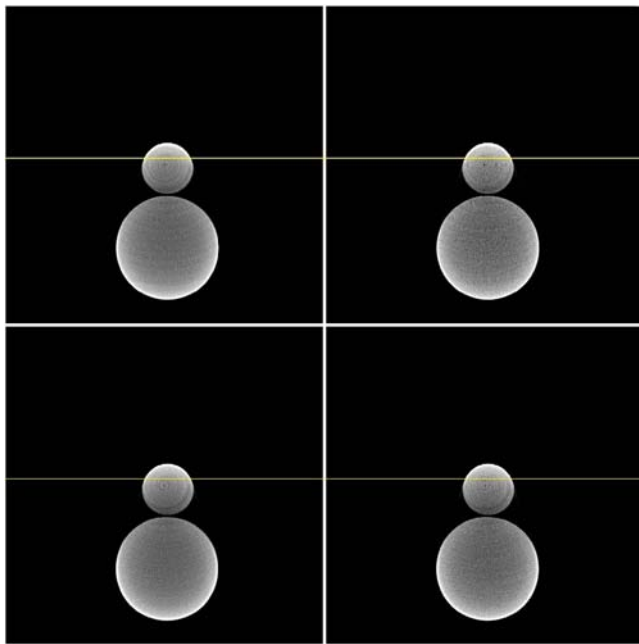
FIG. 8. Slice images of the lucite phantom reconstructed by use of FDK (left) and BPF (right) algorithms within the midplane at $z=0$ (top) and an off-mid plane at $z=0.5$ cm (bottom) from nontruncated data. The display window is [0.5 cm^{-1}, 1.5 cm^{-1}].

FIG. 10. Slice images of the smaller cylinder of the lucite phantom reconstructed by use of FDK (left) and BPF (right) algorithms within the midplane at $z=0$ (top) and an off-midplane at $z=0.5$ cm (bottom) from truncated data. The display window is [0.5 cm^{-1}, 1.5 cm^{-1}].

proposed algorithm. A 5.8 cm reconstruction FOV was used for full image reconstruction from nontruncated data set. We display the reconstructed full images at midplane and an off midplane by the two algorithms in Fig. 8. The display window used is [0.5 cm^{-1}, 1.5 cm^{-1}]. This window is selected to present the difference of the reconstructed images in terms of truncation artifacts clearly.

Reconstructed images obtained with the two algorithms from nontruncated data appear to be almost identical. Line profiles along the specified horizontal lines in the images are also shown in Fig. 9 for a more quantitative comparison. Dotted curves represent the line profiles of the images obtained by FDK algorithm and solid curves represent those obtained by BPF algorithm. They agree within a negligible difference.

A cupping artifact, in which the image has enhanced pixel values at the edge and decreased values at the center, is prominently observed throughout the images. This is due to

scatter and beam hardening of the x-ray beam.[28] In this work, however, correction for the cupping artifact has not been attempted since the existence of the cupping artifact does not compromise the goal of this paper. Ring artifact is also observable in the images, which is dominantly due to nonuniform response of the detector.

For ROI image reconstruction, a 1.6 cm reconstruction FOV was used. Projection data outside of the FOV for each view have been manually deleted to produce data truncation. Therefore, only one third of columns in the middle of the original projection data matrix remains for ROI image reconstruction. We display the reconstructed ROI images at midplane and an off midplane by the two algorithms from the truncated data in Fig. 10 with the same display window as used in Fig. 8. Line profiles along the specified horizontal lines in the images are also shown in Fig. 11. Data truncation artifacts are present in the images reconstructed by FDK algorithm. To compare the images reconstructed by the PI-line-based BPF algorithm from nontruncated and truncated data,
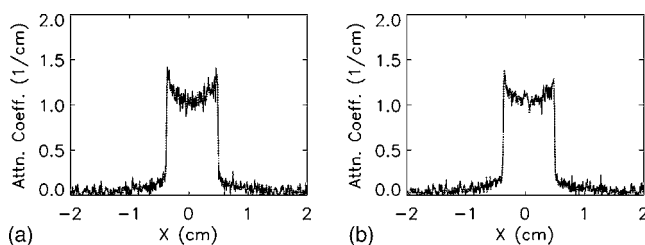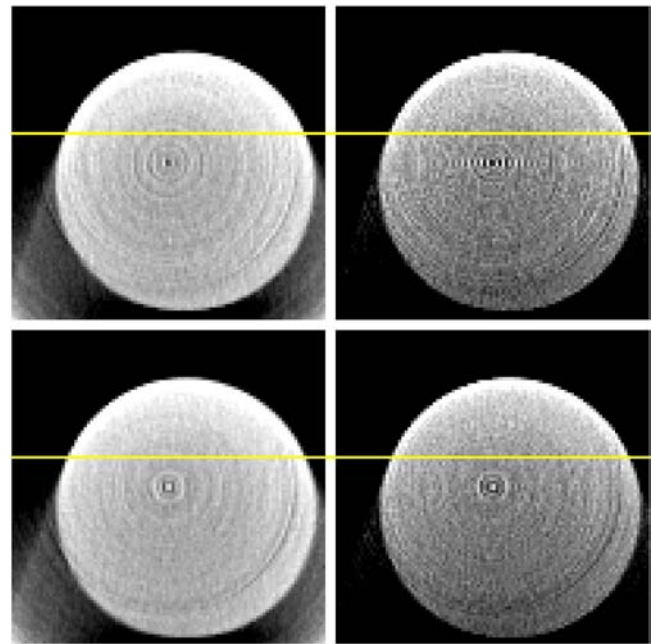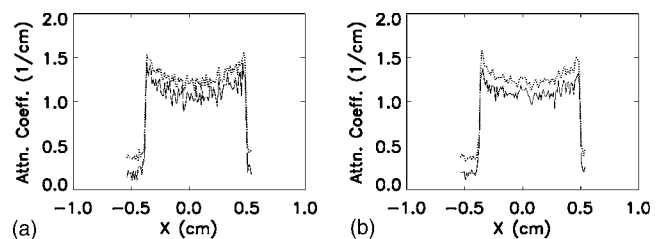

FIG. 9. Profiles along the white horizontal lines indicated in Fig. 8 for reconstructed images (a) at the midplane and (b) at the off-midplane. Dotted curves represent the results obtained from FDK algorithm and solid curves from BPF algorithm. Dotted curves are hardly seen because of the excellent overlap with solid curves.

FIG. 11. Profiles along the white horizontal lines indicated in Fig. 10 for reconstructed images (a) at the midplane and (b) at the off midplane. Dotted curves represent the results obtained from FDK algorithm and solid curves from BPF algorithm.
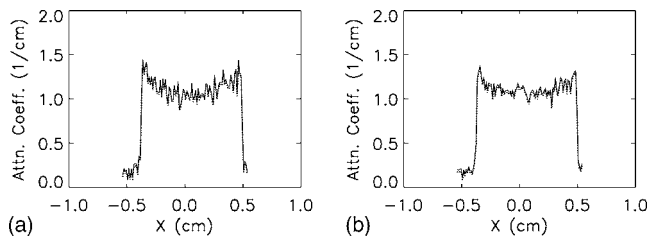
FIG. 12. Profiles along the white horizontal lines indicated in Fig. 8 and in Fig. 10 for reconstructed images by use of the BPF algorithm (a) at the midplane and (b) at the off-midplane from nontruncated data and from truncated data. Dotted curves represent the results obtained from truncated data and solid curves from nontruncated data.

the line profiles along the previously specified lines are plotted in Fig. 12. Dotted curves represent the line profiles of the images obtained from truncated data and solid curves represent those obtained from nontruncated data. Two curves show a good agreement, which implies the successful ROI image reconstruction from truncated data by use of the PI-line-based BPF algorithm.

IV.B. Mouse with FSa fibrosarcoma studies

The second object used to validate the proposed algorithm was a formalin-fixed mouse with an FSa fibrosarcoma on one leg. FSa fibrosarcoma is one kind of soft-tissue tumor grown specifically in mice and rats. The full-scan projection data sets were acquired at a radius of 37.1 cm for the circular trajectory, and at 57.2 cm source-to-detector distance. Three hundred sixty projection views spaced by 1° were again obtained. A 5 cm reconstruction FOV was used for full image reconstruction from nontruncated data. A 2 cm reconstruction FOV was used for ROI image reconstruction from truncated data. Image reconstructions were performed both for nontruncated and truncated data with a FDK algorithm and the PI-line-based BPF algorithm. Figure 13 shows two-dimensional (2D) slice images reconstructed with the FDK algorithm left and the BPF algorithm right from nontruncated data, at midplane top and at an off-midplane bottom. The display window used is $[0.2 \text{ cm}^{-1}, 2.5 \text{ cm}^{-1}]$. Reconstructed images from the two algorithms using nontruncated data again appear to be almost identical. Line profiles along the specified horizontal lines in the images are shown in Fig. 14 for more quantitative comparison. Dotted curves represent the line profiles of the images obtained by FDK algorithm and solid curves represent those obtained by BPF algorithm. They agree within a negligible difference.

Figure 15 shows 2D slice images reconstructed with the FDK algorithm (left) and the BPF algorithm (right) from truncated data, at midplane (top) and at an off-midplane (bottom). With the same display window of $[0.2 \text{ cm}^{-1}, 2.5 \text{ cm}^{-1}]$, it is clearly observed that the images produced by FDK algorithm have increased pixel values compared with those by BPF algorithm. Line profiles along the specified horizontal lines in the images are shown in Fig. 16. Again dotted curves represent the line profiles of the images obtained by FDK algorithm and solid curves represent those obtained by BPF
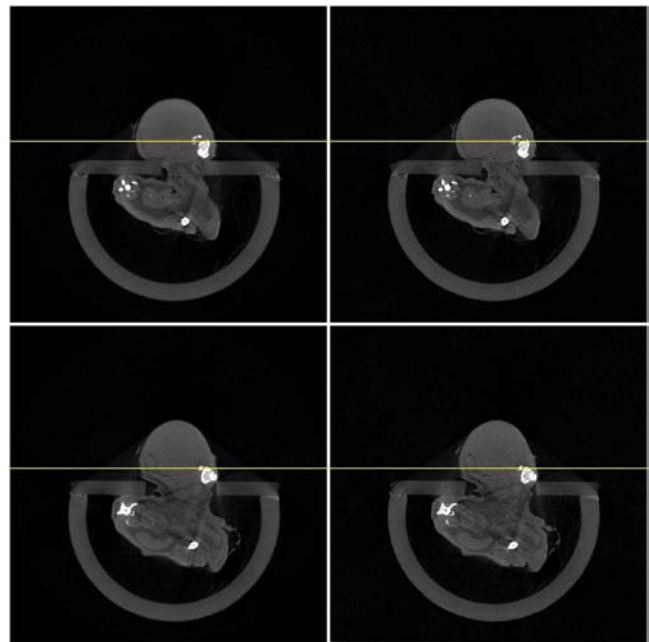

FIG. 13. Slice images of the mouse with FSa fibrosarcoma reconstructed by use of FDK (left) and BPF (right) algorithms within the midplane at $z=0$ (top) and an off-midplane at $z=0.25$ cm (bottom) from nontruncated data. The display window is $[0.2 \text{ cm}^{-1}, 2.5 \text{ cm}^{-1}]$.

algorithm. To compare the images reconstructed by the BPF algorithm from nontruncated data and from truncated data, the line profiles along the previously specified lines are plotted in Fig. 17. Dotted curves represent the line profiles of the images obtained from truncated data and solid curves represent those obtained from nontruncated data. The two curves are in a good agreement.

IV.C. Enhancement of spatial resolution

In previous sections, the PI-line-based BPF algorithm's capability of reconstructing ROI images without truncation artifacts from truncated projection data has been demonstrated experimentally. In this section, this capability of the BPF algorithm is utilized to increase detector sampling density by use of geometric magnification of the imaged object thereby enhancing the spatial resolution of the ROI image without degrading image contrast.
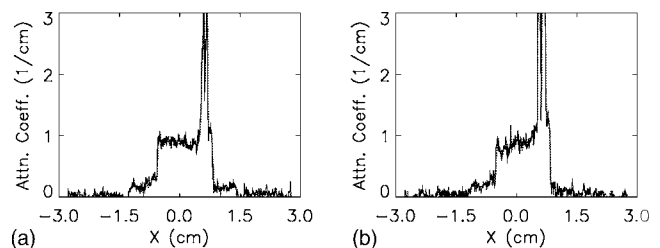

FIG. 14. Profiles along the white horizontal lines indicated in Fig. 13 for reconstructed images (a) at the midplane and (b) at the off-midplane. Dotted curves represent the results obtained from FDK algorithm and solid curves from BPF algorithm.
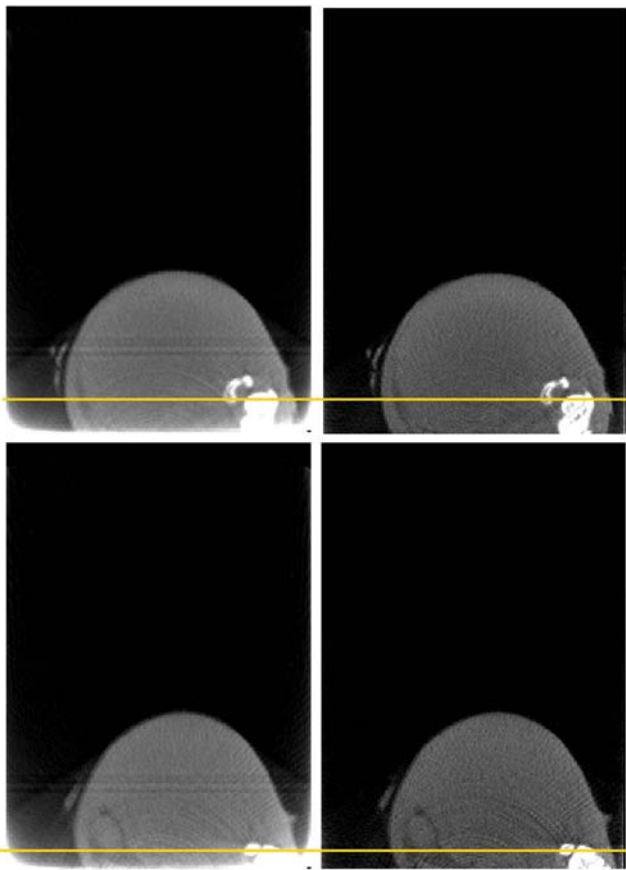
FIG. 15. Slice images of the mouse leg bearing FSa fibrosarcoma reconstructed by use of FDK (left) and BPF (right) algorithms within the midplane at $z=0$ (top) and an off-midplane at $z=0.2$ cm (bottom) from truncated data. The display window is $[0.2$ cm^{-1}, 2.5 cm$^{-1}]$.

In order to quantitatively assess the spatial resolution in the reconstructed images, specially designed phantoms such as a bar phantom have to be used in the evaluation study. However, since those phantoms may not be adequate for our ROI imaging geometry, we have used a mouse having an osteosarcoma on one leg which has relatively detailed features of the bony structure developed by the osteosarcoma. Only a qualitative, graphical interpretation of the reconstructed images in terms of spatial resolution, therefore, is presented in this paper. Quantitative analysis of the enhancement of the spatial resolution due to geometric magnification
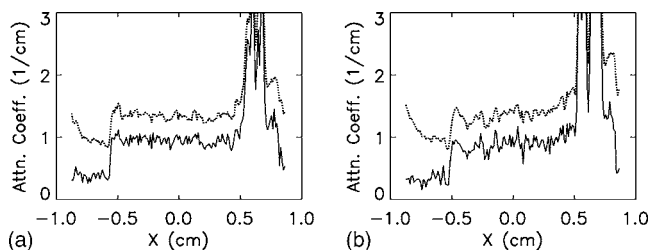

FIG. 16. Profiles along the white horizontal lines indicated in Fig. 15 for reconstructed images (a) at the midplane and (b) at the off-midplane. Dotted curves represent the results obtained from FDK algorithm and solid curves from BPF algorithm.
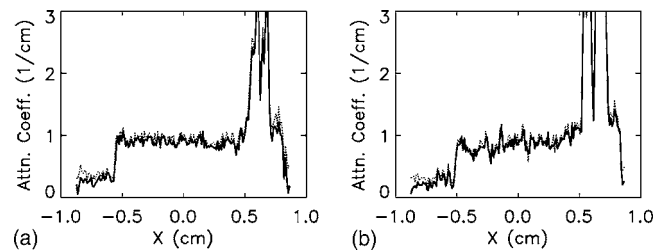

FIG. 17. Profiles along the white horizontal lines indicated in Fig. 13 and in Fig. 15 for reconstructed images by use of the BPF algorithm (a) at the midplane and (b) at the off-midplane from nontruncated data and from truncated data. Dotted curves represent the results obtained from truncated data and solid curves from nontruncated data.

can be found elsewhere,[23] although the data acquisition geometry and the image reconstruction algorithm are different from the ones used in this work. Note that the data acquired in the geometry described in Ref. 23 is not truly truncated because the truncated projection rays in one view are always compensated for from the conjugate view as shown in Fig. 18(a). In comparison, the geometry used in this work produces truly truncated data, with respect to the entire object not to the ROI, where some rays are not sampled by the source and detector in any view as shown in Fig. 18(b). The image reconstruction algorithm used in Ref. 23 therefore cannot be used for ROI image reconstruction as described here. However, the results of Ref. 23 can be considered effective in this paper since the physics of spatial resolution enhancement in both studies stem from the same origin of geometric magnification.

The leg bearing the osteosarcoma is considered as the ROI. Two projection data sets were prepared; 360 projection
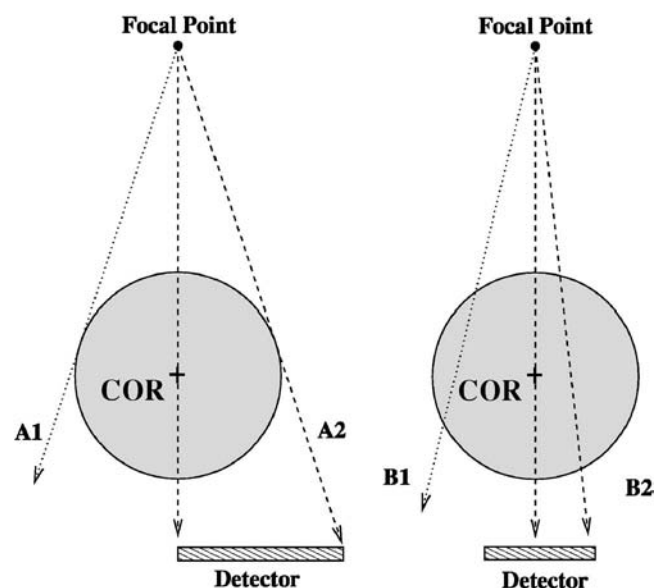

FIG. 18. Tomographic acquisitions with truncated data. The geometry in (a) shows the system geometry used in the paper by Pan (Ref. 23). In this configuration, both "Ray A1" (dotted line) and "Ray A2" (dashed line) are recorded in alternate views of the source and detector. In comparison, (b) shows the geometry used in this work, where some rays (e.g., "Ray B1") are not sampled by the source and detector at any view.

views spaced by 1° were obtained for both of them. One data set was acquired at the radius of 37.1 cm for the circular trajectory, and at 57.2 cm source-to-detector distance. The other projection data set was acquired at the radius of 16.7 cm for the circular trajectory, and at 57.2 cm source-to-detector distance. Therefore, the geometric magnification factor increases from about 1.5 for the first data set to about 3.5 for the second, which is directly related to the increase of data sampling density. As a result of this increase in geometric magnification, data truncation occurs in the second data set, i.e., part of the whole mouse is not illuminated at all projection angles. However, the ROI is always within the FOV. Note the first data set is complete, i.e., no data truncation exists.

From the first projection data set which is complete, the ROI image on a slice is reconstructed on 220×110 image matrix whose pixel size is about 20×20 μm^2 by use of the FDK algorithm. The pixel size was chosen to be small enough to effectively visualize the difference of the spatial resolution of the images. Spatial resolution of an image can be affected also by window function such as Hamming window in the filtering process of the FDK algorithm.[26] We used the Ram-Laks filter to incorporate high frequency components without using any smoothing window. The reconstructed image is displayed in Fig. 19(a) with the display window of [0.1 cm^{-1}, 5.0 cm^{-1}].

From the second data set which includes data truncation, the ROI slice image which corresponds to the slice-image in Fig. 19(a) is reconstructed on the image matrix of the same size by the PI-line-based BPF algorithm and also by the FDK algorithm. The reconstructed images are shown in Figs. 19(b) and 19(c), respectively. One can see that more details of the bony structure are reconstructed in 19(b) than in 19(a) due to higher data sampling density from geometric magnification. It is also observable that the image contrast in 19(c) is severely degraded due to truncation artifacts while it is not in 19(b).

V. DISCUSSION

In this work, we have applied the PI-line-based BPF algorithm to reconstructing ROI images from truncated cone-beam data acquired with a microCT system. In particular, we have qualitatively demonstrated how the proposed algorithm's capability of reconstructing ROI images from truncated data can be exploited to potentially enhance image spatial resolution. A uniform lucite phantom and a mouse one of whose legs bears FSa fibrosarcoma have been involved in the validation of the proposed method. The key point of validation is to show that the PI-line-based BPF algorithm can reconstruct ROI images, from truncated data, with comparable image quality to that of the images reconstructed from complete data. The ROI images reconstructed by use of the FDK algorithm from truncated cone-beam data suffer from truncation artifacts while the ROI images reconstructed by the PI-line-based BPF algorithm from truncated cone-beam data are free from truncation artifacts.
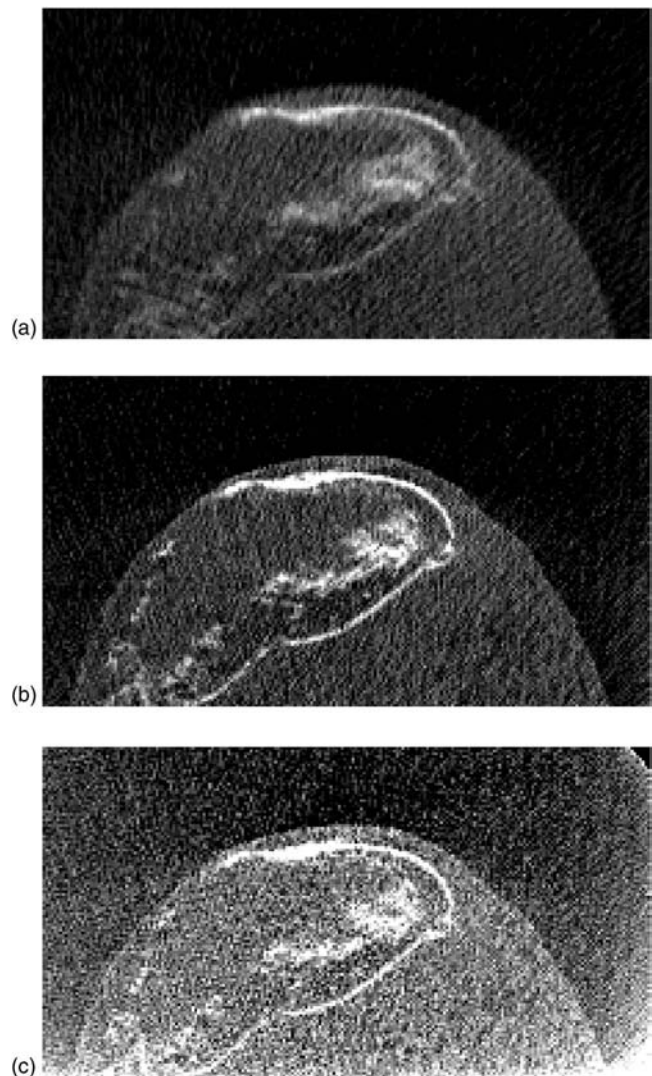

FIG. 19. Slice images of the mouse leg bearing osteosarcoma reconstructed (a) by the FDK algorithm from the complete data set with lower geometric magnification, (b) by the PI-line-based BPF algorithm from the truncated data set with higher geometric magnification, and (c) by the FDK algorithm from the truncated data set with higher geometric magnification. The display window is [0.1 cm^{-1}, 5.0 cm^{-1}].

Empirical correction algorithms, including the extrapolation method,[29] have been developed for compensating for nonsevere truncations. It may be, however, difficult to correct for severe truncations that are encountered in ROI scans, as described here for small animal imaging. The BPF algorithm does not involve any correction procedures in reconstructing accurate ROI images. As compared to the zoom-in method utilizing two projection data sets, one of which is obtained with a full FOV scan and the other obtained with a limited FOV scan with a larger magnification, the proposed ROI imaging approach may have several advantages. Scan time can be reduced to, at least, less than half of that time required by the zoom-in method. More importantly, one can substantially reduce the overall x-ray exposure as compared to that in the zoom-in method. Because the BPF algorithm requires data from x-ray illumination that covers only the

ROI at the necessary views, one can further reduce the imaging-radiation dose and scatters if appropriate x-ray illumination collimation is used. However, the precise determination of x-ray exposure for each view should be conducted through careful studies of the ROI image quality, which is beyond the scope of this work.

Enhancement of spatial resolution due to geometric magnification is limited by a finite size of the x-ray focal spot. As noted by Kruger *et al.*,[30] the spatial resolution of a digital imaging system is maximized when the image of the focal spot projected through a point in the object plane onto the image plane just covers the width of two pixels, i.e., when $a(m-1)=2d$. Here, a and d denote the focal spot size and the detector pixel size, respectively, and m represents the geometric magnification of the system. The microCT system used in this work allows up to $m=6$ from this calculation with $a=20$ μm and $d=50$ μm. In such a high magnification case, the data truncation problem would become even more severe, whereas the PI-line-based BPF algorithm for ROI image reconstruction would be able to allow such a choice of the magnification.

It should be pointed out that the ROI imaging problems under study differ from the interior problem in which the ROI contains no boundary of the subject. Other artifacts such as beam hardening, scatter, and metal artifacts should be appropriately corrected for reconstructing more accurate images, which will be pursued in our future studies.

ACKNOWLEDGMENTS

[a)]E-mail: xpan@uchicago.edu

[1]E. L. Ritman, "Molecular imaging in small animals—roles for micro-CT," J. Cell. Biochem. **39**, 116–124 (2002).

[2]N. L. Ford, M. M. Thomton, and D. W. Holdsworth, "Fundamental image quality limits for microcomputed tomography in small animals," Med. Phys. **30**, 2869–2877 (2003).

[3]S.-C. Lee, H.-K. Kim, I.-K. Chun, M.-H. Cho, S.-Y. Lee, and M.-H. Cho, "A flat-panel detector based micro-CT system: Performance evaluation for small-animal imaging," Phys. Med. Biol. **48**, 4173–4185 (2003).

[4]F. Kiessling, S. Greschus, M. P. Lichy, M. Bock, C. Fink, S. Vosseler, J. Moll, M. M. Mueller, N. E. Fusenig, H. Traupe, and W. Semmler, "Volumetric computed tomography (VCT): A new technology for noninvasive, high-resolution monitoring of tumor angiogenesis," Nature Medicine **10**, 1133–1138 (2004).

[5]M. Marxen, M. M. Thornton, C. B. Chiarot, G. Klement, J. Koprivnikar, J. G. Sled, and R. M. Henkelman, "MicroCT scanner performance and considerations for vascular specimen imaging," Med. Phys. **31**, 305–313 (2004).

[6]C. T. Badea, B. Fubara, L. W. Hedlund, and G. A. Johnson, "4-D micro-CT of the mouse heart," Mol. Imag. **4**, 110–116 (2005).

[7]D. Cavanaugh, E. Johnson, R. E. Price, J. Kurie, E. L. Travis, and D. D. Cody, "In vivo respiratory-gated micro-CT imaging in small-animal on-

[8]E. B. Walters, K. Panda, J. A. Bankson, E. Brown, and D. D. Cody, "Improved method of *in vivo* respiratory-gated micro-CT imaging," Phys. Med. Biol. **49**, 4163–4172 (2004).

[9]A. B. Hwang and B. H. Hasegawa, "Attenuation correction for small animal SPECT imaging using x-ray CT data," Med. Phys. **32**, 2799–2804 (2005).

[10]A. Faridani, D. V. Finch, E. L. Ritman, and K. T. Smith, "Local tomography II," SIAM J. Appl. Math. **57**, 1095–1127 (1997).

[11]P. Kuchment, K. Lancaster, and L. Mogilevskaya, "On local tomography," Inverse Probl. **11**, 571–589 (1995).

[12]E. L. Ritman, J. H. Dunsmuir, A. Faridani, D. V. Finch, K. T. Smith, and P. J. Thomas, "Local reconstruction applied to X-ray microtomography," in *IMA Volumes in Mathematics and Its Applications, Inverse Problems in Wave Propagation*, G. Chavent, G. Papanicolaov, P. Sacks, and W. Symes, Eds. 1997 (Springer-Verlag, New York, 1997), pp. 443–452.

[13]I. K. Chun, M. H. Cho, S. C. Lee, M. H. Cho, and S. Y. Lee, "X-ray micro-tomography system for small-animal imaging with zoom-in imaging capability," Phys. Med. Biol. **49**, 3889–3902 (2004).

[14]F. Noo, M. Defrise, R. Clackdoyle, and H. Kudo, "Image reconstruction from fan-beam projections on less than a short scan," Phys. Med. Biol. **47**, 2525–2546 (2002).

[15]H. Kudo, F. Noo, M. Defrise, and R. Clackdoyle, "New super-short-scan algorithms for fan-beam and cone-beam reconstruction," in *IEEE Medical Imaging Conference Record*, S. D. Metzler, Ed., Norfolk, Virginia, 2002, pp. M5–3.

[16]X. Pan, D. Xia, Y. Zou, and L. Yu, "A unified analysis of FBP-based algorithms in helical cone beam and circular cone- and fan-beam scans," Phys. Med. Biol. **49**, 4349–4369 (2004).

[17]G. Chen, "A new framework of image reconstruction from fan beam projections," Med. Phys. **30**, 1151–1161 (2003).

[18]Y. Zou and X. Pan, "Image reconstruction on PI-lines by use of filtered backprojection in helical cone-beam CT," Phys. Med. Biol. **49**, 2717–2731 (2004).

[19]Y. Zou and X. Pan, "An extended data function and its backprojection onto PI-lines in helical cone-beam CT," Phys. Med. Biol. **49**, N383–N387 (2004).

[20]Y. Zou, X. Pan, and E. Y. Sidky, "Image reconstruction in regions-of-interest from truncated projections in a reduced fan-beam scan," Phys. Med. Biol. **50**, 13–27 (2005).

[21]L. Yu, Y. Zou, E. Y. Sidky, and X. Pan, "Region of interest reconstruction from truncated data in circular cone-beam CT," IEEE Trans. Med. Imaging **25**, 869–881 (2006).

[22]M. King, X. Pan, L. Yu, and M. Giger, "Region-of-interest reconstruction of motion-contaminated data using a weighted backprojection filtration algorithm," Med. Phys. **33**, 1222–1238 (2006).

[23]X. Pan, L. Yu, and C.-M. Kao, "Spatial-resolution enhancement in computed tomography," IEEE Trans. Med. Imaging **24**, 246–253 (2005).

[24]P. E. Danielsson, P. Edholm, and M. Seger, "Towards exact 3D-reconstruction for helical cone-beam scanning of long objects. A new detector arrangement and a new completeness condition," in *Proceedings of the 1997 International Meeting on Fully Three-Dimensional Image Reconstruction in Radiology and Nuclear Medicine*, D. W. Townsend and P. E. Kinahan, Eds., Pittsburgh, 1997, pp. 141–144.

[25]X. Pan, Y. Zou, and D. Xia, "Peripheral and central ROI-image reconstruction from and data-redundancy exploitation in truncated fan-beam data," Med. Phys. **32**, 673–684 (2005).

[26]J. Hsieh, *Computed Tomography-Principles, Designs, Artifacts, and Recent Advances* (SPIE Press, Bellingham, WA, 2003).

[27]S. Cho, J. Bian, C. A. Pelizzari, J. S. Souris, C. T. Chen, and X. Pan, "Performance evaluation of a prototype microCT," in *IEEE Medical Imaging Conference Record*, San Diego, 2006, pp. M14–183.

[28]L. Zhang, H. Gao, S. Li, Z. Chen, and Y. Xing, "Cupping artifacts analysis and correction for a FPD-based cone-beam CT," in *Computational Imaging IV. Proceedings of the SPIE*, C. A. Bouman, E. L. Miller, and I. Pollak, Eds., 2006, Vol. 6065, pp. 282–291 (unpublished).

[29]B. Ohnesorge, T. Flohr, K. Schwartz, J. P. Heiken, and K. T. Bae, "Efficient correction for CT image artifacts caused by objects extending outside the scan field of view," Med. Phys. **27**, 39–48 (2000).

[30]R. A. Kruger, C. A. Mistretta, and S. J. Riederer, "Physical and technical considerations of computerized fluoroscopy difference imaging," IEEE Trans. Nucl. Sci. **NS-28**, 205–212 (1981).

Submit to: MI01, Hsieh, Samei
Title of Conference: PHYSICS OF MEDICAL IMAGING
Intensity-weighted region-of-interest imaging in cone-beam CT
[1]The University of Chicago, Department of Radiology, Chicago, IL 60637
[2]The University of Chicago, Department of Radiation & Cellular Oncology, Chicago, IL 60637
[1,2]Seungryong Cho: Phone 773-834-8061, srcho@uchicago.edu
[1]Dan Xia: Phone 773-834-9051, danxia@uchicago.edu
[2]Charles A. Pelizzari: Phone 773-702-1688, c-pelizzari@uchicago.edu
[1]Xiaochuan Pan: Phone 773-702-1293, xpan@uchicago.edu
Oral Presentation

Purpose   Cone-beam CT (CBCT) is becoming increasingly popular in image-guided radiation therapy (IGRT) partly due to its relatively abundant image information and its convenience in use. Target positioning is one of the most important steps in IGRT procedures, and one of the points of using CBCT is to determine the day-to-day position of the target and surrounding normal tissues inside the patient [1]. Accurate image of the target is an essential ingredient in the task of target positioning. Moreover, in most IGRT procedures, it is desirable to have accurate image of the target while sparing patient dose specifically to the normal tissue outside the target. This issue becomes more important when there are radiation sensitive tissues near the treatment target. Accurate, region-of-interest (ROI) imaging technique in this regard is an important, prospective candidate for routine CBCT in IGRT. An ROI imaging here is meant to imply that only the projection data of the given ROI is taken for each view, thereby reducing the dose to the outside of the ROI.

Recently developed, the chord-based backprojection-filtration (BPF) algorithm is well known to produce accurate images of certain ROI's in general CBCT scanning configurations. Data truncation artifacts, often appearing in the reconstructed images by conventional algorithms, can be avoided by use of the chord-based BPF algorithm in many ROI imaging tasks. However, some ROI imaging tasks such as interior problems cannot be addressed even by the chord-based BPF algorithm. But, it is likely that most imaging targets are embedded inside the body, which invokes the interior problem. Therefore, we propose an innovative, intensity-wighted region-of-interest (IWROI) imaging technique to reduce the imaging dose to the outside of the imaging target while maintaining the imaging problem solvable by the chord-based BPF algorithm. In this work, we focus on circular CBCT which is the dominant imaging modality employed in most radiation therapy systems although the idea can be extended to any general scanning configurations such as saddle trajectory. We have conducted numerical studies to validate our proposed method.

Methods   We would like to note that a circular scanning geometry does not satisfy data sufficiency condition, often referred to as the Tuy's condition, for points lying off the mid-plane. We have introduced virtual chord concept to apply chord-based algorithms to reconstruct the images on the off-mid-plane where the Tuy's condition is not met [2]. Comparable image quality was reported from the virtual chord-based algorithms to that obtained by a conventional Feldkamp-Davis-Kress (FDK) -type algorithm when there is no transverse projection data truncation. When transversely truncated data were used, BPF-type virtual chord-based algorithm was shown to perform ROI imaging at the level of the same image quality as when nontruncated data were used. FDK-type algorithm, however, produced ROI images with typical truncation artifacts. This is the key feature of the chord-based BPF algorithm. Another important feature that makes the IWROI feasible is the fact that the noise from the outer ROI does not propagate significantly into the inner ROI due to noise transfer property of the Hilbert transform.

The ROI in this task is divided into two subROI's. Higher dose is delivered to the inner ROI containing the target, and lower dose is to the outer ROI. Each projection image, therefore, will have different noise levels in two regions: inner ROI projection and outer ROI projection. Fig. 1 shows a schematic of the proposed scanning geometry. The prototype circular CBCT scanning geometry is assumed in this work where the source and the detector are fixed, and the object is rotating around the axis. Outer ROI is determined by the collimator opening, which is typically limited by the detector size. Inner ROI is determined by the filter opening, which is selected to illuminate the target specifically with higher beam intensity than that used for outer ROI. From the intensity variation of the x-ray beam, different noise levels at inner and outer ROI regions are expected. Therefore, in the numerical study, different Gaussian noise levels were used in the projection data for inner ROI and for outer ROI. Even though we only show an example of static collimation and static filtration in this work, the IWROI technique can be extended to more arbitrary shape of the ROI provided that dynamic collimation and filtration are available.

Results   A uniform ellipsoid phantom was used as an imaging subject with three different combination of the noise levels in the inner and the outer ROI's. The noise level, or the standard deviation of a Gaussian noise, of the inner ROI was fixed by 0.1 and those of the outer ROI were varied by 0.5,1.0, and 2.0. Numerical simulation results are shown in Fig. 3. The profiles along the mid-lines of the images are plotted in Fig. 3(d). It can be observed that the outer ROI noise level rarely affect the inner ROI noise level. Note also that the images, reconstructed from truncated projection data by the chord-based BPF algorithm, have no truncation artifacts.
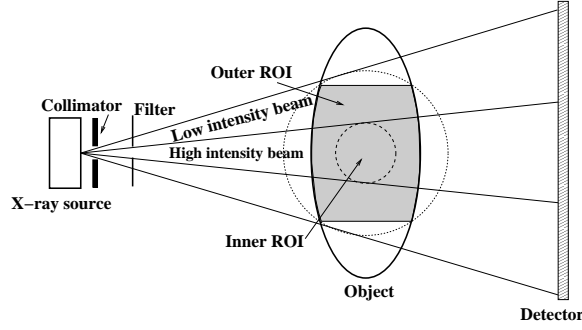
<div align="center">1</div>

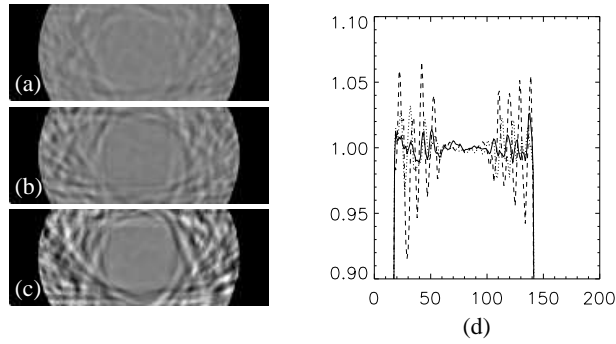Figure 1: Schematic of the proposed, intensity-weighted ROI scanning.

Figure 2: Reconstructed images of the uniform phantom with its inner ROI noise level of 0.1 and its outer ROI noise level of (a) 0.5, (b) 1.0, and (c) 2.0. Display window is [0.9,1.1]. The profiles along the middle, horizontal lines in the images are plotted in (d). Solid line represents (a), dotted line (b), and dashed line represents (c).

To compare with the FDK algorithm, the Shepp-Logan phantom was used as an imaging object and the projection data were prepared to have data truncation. As shown in Fig. 3, the image reconstructed by FDK-type algorithm contains typical truncation artifacts throughout the whole image: pixel values are increased and the amount of pixel value inflation increases as it approaches the truncated boundary of the image. The image reconstructed by chord-based BPF algorithm, however, is free from truncation artifacts.

New work The proposed technique can be considered as an analogy of the intensity-modulated radiation therapy (IMRT). As concerns about the patient dose due to repeated CT scanning become serious, the proposed method can contribute significantly to reducing the patient dose. The intensity variation concept has been already used in diagnostic imaging research including Ref. [3], but their image reconstruction method is soley based on FDK algorithm. Our work can be much more flexibly applied to the ROI problem that may have severe data truncation.

Conclusion An ROI CBCT with intensity-weighting technique is presented. Accurate image information of the target is required for IGRT, and it is desirable to reduce dose delivered to the normal tissue surrounding the target. Our proposed method can reconstruct the target image with high signal-to-noise ratio and the surrounding tissue image with relatively low SNR. Data truncation artifacts can be avoided by using the proposed, chord-based BPF-type algorithm, and noise propagation from the normal tissue region to the target region is well-suppressed due to the property of Hilbert transform. The proposed algorithm is a promising technique in CBCT for IGRT. Experiments are in progress.
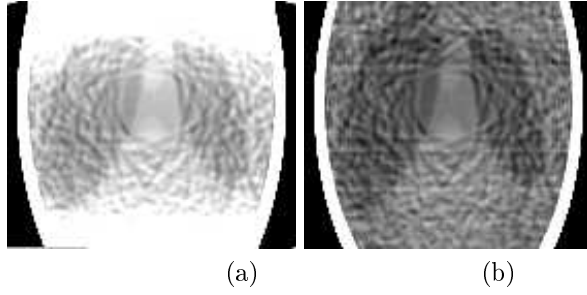
(a)   (b)

Figure 3: Numerical images of the intensity-weighted ROI by (a) FDK and (b) BPF algorithms. Display window is [0.95,1.1].

References

[1] D. A. Jaffray, "Emergent technologies for 3-dimensional image-guided radiation delivery," *Semin. Radiat. Oncol.*, vol. 15, pp. 208–216, 2005.

[2] L. Yu, Y. Zou, E. Y. Sidky, and X. Pan, "Region of interest reconstruction from truncated data in circular cone-beam CT," *IEEE Trans. Med. Imag.*, vol. 25, pp. 869–881, 2006.

[3] R. Chityala, K. R. Hoffmann, S. Rudin, and D. R. Bednarek, "Region of interest computed tomography: Comparison with full field of view and truncated ct for a human head phantom," *Proc. SPIE*, vol. 5745, pp. 583–590, 2005.

Submit to: MI01, Hsieh, Samei

Title of Conference: PHYSICS OF MEDICAL IMAGING

Few-view cone-beam computed tomography for image-guided radiation therapy

'[1]The University of Chicago, Department of Radiology, Chicago, IL 60637

[2]The University of Chicago, Department of Radiation & Cellular Oncology, Chicago, IL 60637

[1,2]Seungryong Cho: Phone 773-834-8061, srcho@uchicago.edu

[1]Emil Y. Sidky: Phone 773-834-7845, sidky@uchicago.edu

[2]Charles A. Pelizzari: Phone 773-702-1688, c-pelizzari@uchicago.edu

[1]Xiaochuan Pan: Phone 773-702-1293, xpan@uchicago.edu
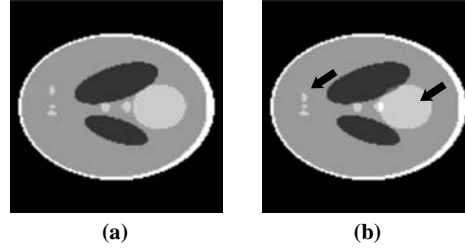
Oral Presentation

(a) **(b)**

Figure 1: (a) A prior image and (b) the shifted image. Two arrows indicate the internal structures that have moved.

Purpose Cone-beam computed tomography (CBCT) has been actively investigated and developed for providing accurate, timely images of the treatment target in image-guided radiation therapy (IGRT) [1]. Especially, the recently available kV cone-beam imaging capability of a linear accelerator system provides excellent soft-tissue contrast, which is an important benefit in IGRT of such as prostate cancer. Reduction of the treatment margins owing to improved image quality of the target would increase the conformality of dose distribution in a fractionated treatment where day-to-day, inter-fraction organ motion is present. However, radiation dose accumulated to the patient due to daily CBCT before each fractionated treatment may pose a challenge in the patient's radiation safety. This motivated our work to develop a few-view CBCT for IGRT, where few-view means a limited number of projection views out of 360° in a circular scan.

Recently, we have developed an iterative image reconstruction algorithm based on total-variation (TV) minimization from incomplete cone-beam projection data. In numerical studies with a variety of incomplete cone-beam data sets including truncated data, reduced scan range, and sparse sampling, the developed algorithm, which is referred to as TV algorithm hereafter, showed an excellent performance compared with existing algorithms such as algebraic reconstruction technique (ART) and expectation maximization (EM) [2]. The TV algorithm begins in general with a uniform image as an initial guess, and goes through iteration steps to minimize the image TV. In an IGRT, a patient usually undergoes a CT scanning for treatment planning, which can provide the reference image for image-guidance procedure. Therefore, in this work, we propose a TV algorithm with *a priori* information in few-view CBCT for IGRT.

Only preliminary numerical study has been made yet, and the feasibility of the proposed algorithm and the future work will be discussed in this paper.

Methods In order to see the feasibility of the proposed algorithm, we have conducted a numerical study for a 2-D circular, fan-beam geometry in this work. A modified 2-D Shepp-Logan phantom was used as an imaging object, and this phantom was used as an initial guess, i.e. planning-CT image. Two of the internal components of the phantom were shifted. A series of few-view projection data sets of the shifted phantom were prepared, and fed into the TV algorithm with or without the prior information of the original phantom image. Fig. 1 shows the original phantom image and the shifted phantom image emphasizing the change of the internal structures. The projection data sampling was made in an equiangular fashion in this work, which is not a necessary condition nevertheless.

Results The reconstructed images by TV algorithm with and without the prior information from different number of projection images are shown in Figs. 2-4. The images with the prior information are reasonably reconstructed even from 5-view data, where the images without prior appear to become reasonable from 20-view data. This numerical study confirms the prior information can help reducing the required number of views in TV algorithm.

New work For patient positioning and target localization in IGRT, portal images or orthogonal radiographic projection images have been utilized. Digitally-reconstructed-radiographs (DRRs) have been prepared from the planning CT image, and image registration or image matching between DRR and projection images have been performed. In many cases, hard tissue such as bony structure or implants have been chosen
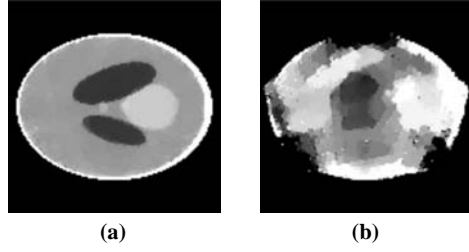
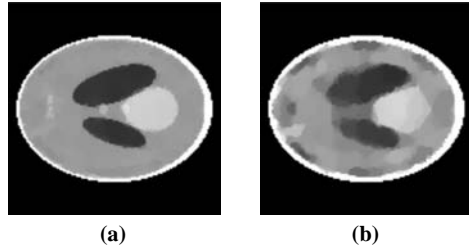Figure 2: Reconstructed images from 5-view data (a) with prior image and (b) without prior image.

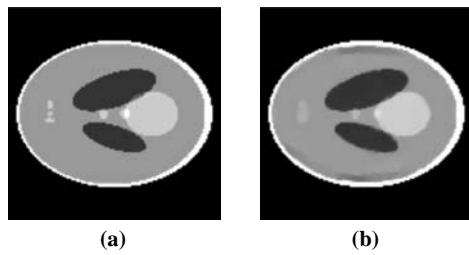Figure 3: Reconstructed images from 10-view data (a) with prior image and (b) without prior image.

Figure 4: Reconstructed images from 20-view data (a) with prior image and (b) without prior image.

2

as matching targets because they are relatively immobile and have higher image contrast. However, these methods cannot compensate for the internal motion and/or shape change of the soft-tissue such as prostate between day-to-day treatments. Even if the soft-tissue can be registered and localized correctly, the treatment plan cannot be replanned based on these radiographic projection images. Since our proposed algorithm can reconstruct 3D volume images of the target, treatment replanning based on the newly reconstructed CT images becomes possible.

Conclusion   The proposed method successfully reconstructed the phantom image from few-view projection data sets with *a priori* image. The results are preliminary and more work needs to be done for validation and for potential applications of the proposed method. Cone-beam projection data have to be used and the reconstructed images by the proposed method from cone-beam data have to be evaluated.

In addition, we may still need an image registration procedure before running our TV algorithm since the algorithm requires the initial guess, or planning CT image, be in the same coordinate with the CBCT system. In this context, we are not negating the existing methods used in patient positioning and target localization, but instead reinforcing them with the advanced function of volumetric image reconstruction. It is remained for our future work to develop an image registration process from the few-view data before reconstructing the volumetric image.

References

[1] D. A. Jaffray, J. H. Siewerdsen, J. W. Wong, and A. A. Martinez, "Flat-panel cone-beam computed tomography for image-guided radiation therapy," *Int. J. Radiat. Oncol. Biol. Phys.*, vol. 53, pp. 1337–1349, 2002.

[2] E. Y. Sidky, C. M. Kao, and X. Pan, "Accurate image reconstruction from few-views and limited-angle data in divergent-beam CT," *J. X-Ray Sci. Tech.*, vol. 14, pp. 119–139, 2006.